DISEASES AND DISORDERS

Mutation-induced DNMT1 cleavage drives neurodegenerative disease

Wencai Wang[1,2†], Xingsen Zhao[3,4,5†], Yanjiao Shao[1], Xiaoya Duan[1], Yaling Wang[1], Jialun Li[1], Jiwen Li[1], Dali Li[1], Xuekun Li[3,4,5]*, Jiemin Wong[1,2]*

Specific mutations within the replication foci targeting sequence (RFTS) domain of human DNMT1 are causative of two types of adult-onset neurodegenerative diseases, HSAN1E and ADCA-DN, but the underlying mechanisms are largely unknown. We generated *Dnmt1-M1* and *Dnmt1-M2* knock-in mouse models that are equivalent to Y495C and D490E-P491Y mutation in patients with HSAN1E, respectively. We found that both mutant heterozygous mice are viable, have reduced DNMT1 proteins, and exhibit neurodegenerative phenotypes including impaired learning and memory. The homozygous mutants die around embryonic day 10.5 and are apparently devoid of DNMT1 proteins. We present the evidence that the mutant DNMT1 proteins are unstable, most likely because of cleavage within RFTS domain by an unidentified proteinase. Moreover, we provide evidence that the RFTS mutation–induced cleavage of DNMT1, but not mutation itself, is responsible for functional defect of mutant DNMT1. Our study shed light on the mechanism of DNMT1 RFTS mutation causing neurodegenerative diseases.

INTRODUCTION

In mammals, DNA methylation is a key epigenetic modification involved in the regulation of gene expression, parental imprinting, chromosome X inactivation, embryonic development, neurogenesis and differentiation, and cellular reprogramming (*1*–*6*). DNA methyltransferase 1 (DNMT1), known as the DNA maintenance methyltransferase that shows a preference for hemimethylated DNA substrate, plays a key role in maintaining the existing patterns of DNA methylation in genome by converting hemimethylated DNA generated during DNA replication to symmetrically fully methylated DNA (*7*–*9*). Consistent with this character, DNMT1 is recruited to DNA replication foci in S phase of the cell cycle, and a conserved RFTS (the replication foci targeting sequence) domain within its large N-terminal region is required for this event (*10*, *11*). Recent studies have elucidated the potential mechanisms by which the RFTS domain targets DNMT1 to replication sites. This involves UHRF1 (ubiquitin-like with plant homeodomain and RING finger domain 1), a multifunctional ubiquitin E3 ligase that is required for DNMT1-dependent DNA methylation (*12*–*16*). UHRF1 itself binds DNA replication sites via its unique ability of binding hemimethylated DNA, histones, and methylated DNA ligase 1 (*15*, *17*–*23*) and catalyzes histone H3 and H2B ubiquitination at DNA replication sites (*11*, *24*, *25*). The RFTS domain of DNMT1 interacts not only with UHRF1 but also with ubiquitinated H3/H2B and ubiquitinated proliferating cell nuclear antigen (PCNA)–associated factor 15 (*11*, *24*–*26*), and these interactions, together with additional interaction between DNMT1 and PCNA, are likely to account for DNMT1 replication site targeting. DNMT1 knockout mice show extensive demethylation of the genome and die shortly after gastrulation, underlying the crucial role of DNMT1 in DNA methylation and early development (*27*). Furthermore, conditional knockout of DNMT1 in the neural precursors in postnatal mice results in severe DNA hypomethylation and substantial loss of neuronal cells, revealing a critical role of DNMT1 and its associated DNA methylation in generation and maintenance of neuronal cells (*4*, *28*, *29*).

While the functional significance of DNMT1 and its associated DNA methylation in development and neurogenesis have long been recognized, DNMT1 mutations have only recently been identified in two related neurodegenerative diseases in human, HSAN1E (hereditary sensory and autonomic neuropathy type 1E with dementia and hearing loss) and ADCA-DN (autosomal dominant cerebellar ataxia, deafness, and narcolepsy) (*30*–*32*). Both diseases are due to autosomal dominantly inherited heterozygous mutations of DNMT1, with characteristics of adult-onset and age-dependent progression (*30*–*32*). So far, all DNMT1 mutations identified in the patients with HSAN1E and ADCA-DN are located in the RFTS domain, with HSAN1E mutations located in the N-terminal or middle of RFTS and with the ADCA-DN mutations in the C-terminal of RFTS (*32*, *33*). Several groups have investigated how various RFTS mutations affect the biological properties of DNMT1 (*30*, *32*, *34*). Protein misfolding, proteasome-dependent premature degradation, reduced methyltransferase activity, mislocalization, and formation of cytoplasmic aggregates have been observed for some mutants in some, but not all, studies (*30*, *32*, *34*). Paradoxically, these cell-based studies also show that the mutant proteins are correctly localized to replication foci during S phase of cell cycle, suggesting that the RFTS function is largely intact (*30*, *32*, *34*). Thus, how the RFTS mutations affect DNMT1 leading to neurological defect remains largely unknown.

Here, we reported the generation and characterization of two Dnmt1 HSAN1E mouse models, M1 with Y500C mutation and M2 with P496Y mutation, that were equivalent to Y495C hotspot mutation and D490E-P491Y mutation found in respective human patients with HSAN1E (Fig. 1A). We demonstrated that the heterozygous mutant mice exhibit the symptoms of neurodegeneration and that the

[1]Shanghai Key Laboratory of Regulatory Biology, Fengxian District Central Hospital–ECNU Joint Center of Translational Medicine, Institute of Biomedical Sciences and School of Life Sciences, East China Normal University, Shanghai 200241, China. [2]Joint Center for Translational Medicine, Fengxian District Central Hospital, 6600th Nanfeng Road, Fengxian District, Shanghai 201499, China. [3]The Children's Hospital, School of Medicine, Zhejiang University, Hangzhou 310052, China. [4]Institute of Translational Medicine, School of Medicine, Zhejiang University, Hangzhou 310029, China. [5]National Clinical Research Center for Child Health, Hangzhou 310052, China. [6]Key Laboratory of Reproduction Regulation of NPFPC, SIPPR, IRD, Fudan University, Shanghai 200032, China.
*Corresponding author. Email: jmweng@bio.ecnu.edu.cn (J.W.); xuekun_li@zju.edu.cn (X.L.)
†These authors contributed equally to this work.

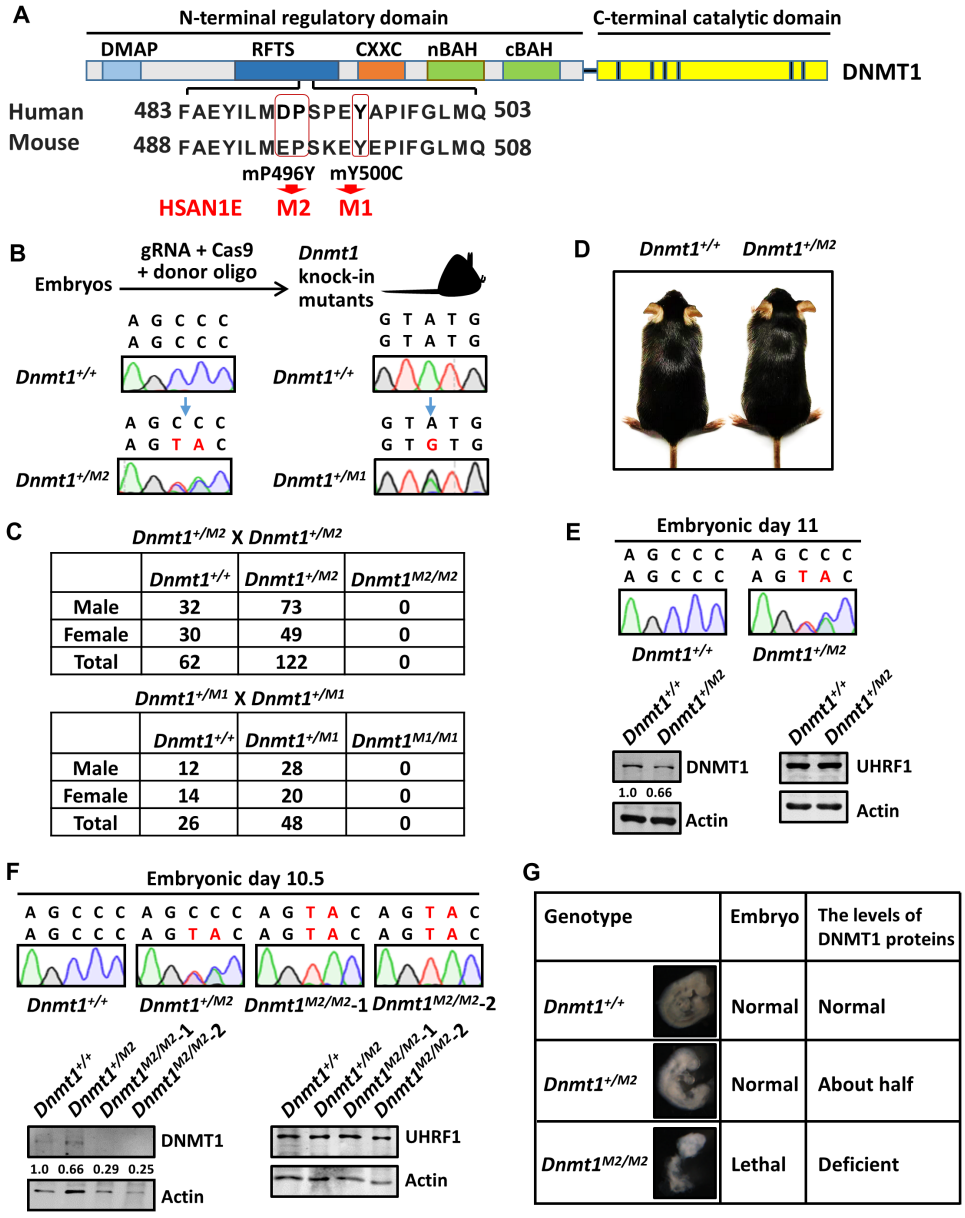

	Dnmt1+/+	Dnmt1+/M2	Dnmt1M2/M2
Male	32	73	0
Female	30	49	0
Total	62	122	0

	Dnmt1+/+	Dnmt1+/M1	Dnmt1M1/M1
Male	12	28	0
Female	14	20	0
Total	26	48	0

Genotype	Embryo	The levels of DNMT1 proteins
Dnmt1+/+	Normal	Normal
Dnmt1+/M2	Normal	About half
Dnmt1M2/M2	Lethal	Deficient

Fig. 1. The homozygous *Dnmt1* RFTS knock-in mice are embryonic lethal. (**A**) Schematic diagram showing two DNMT1 RFTS mutations in patients with HSAN1E selected for generation of knock-in mouse models. The *Dnmt1*-M1 contained Tyr^{500}-to-Cys mutation that is equivalent to the Y495C hotspot mutation in patients with HSAN1E, and Dnmt1-M2 contained Pro^{496}-to-Tyr mutation equivalent to Asp^{490}/Glu-Pro^{491}/Tyr mutation observed in one family of patients with HSAN1E. (**B**) Generation of knock-in mouse models via CRISPR-Cas9 and confirmation of heterozygous mutation by DNA sequencing. (**C**) Summary of numbers of three genotypes obtained through breeding of heterozygous mice. (**D**) Heterozygous mice are grossly normal. Shown are representative $Dnmt1^{+/+}$ and $Dnmt1^{+/M2}$ mice. (**E**) Analysis of embryonic day 11 (E11) embryos derived from mating between $Dnmt1^{+/M2}$ male and female mice. Top: DNA sequencing analysis. Bottom: The levels of DNMT1 and UHRF1 proteins in $Dnmt1^{+/+}$ and $Dnmt1^{+/M2}$ embryos. (**F**) Analysis of E.10.5-day embryos derived from mating between $Dnmt1^{+/M2}$ male and female mice. Top: DNA sequencing analysis identified $Dnmt1^{+/+}$, $Dnmt1^{+/M2}$, and $Dnmt1^{M2/M2}$ embryos. Bottom: The levels of DNMT1 and UHRF1 in the corresponding embryos determined. (**G**) Summary of $Dnmt1^{+/+}$, $Dnmt1^{+/M2}$, and $Dnmt1^{M2/M2}$ embryos.

homozygous mutant mice are embryonic lethal. We found that the mutant DNMT1 proteins are unstable and form aggregates in the nucleolus and this is due to specific cleavage of mutant proteins by an unidentified proteinase. We propose that specific cleavage of mutant DNMT1 proteins and the consequent aberrant nucleolus localization is causal to neurological defects in patients with HSAN1E.

RESULTS

The homozygous *Dnmt1* RFTS knock-in mutant mice are embryonic lethal with severely reduced DNMT1 proteins

To generate mouse models for HSAN1E diseases caused by DNMT1 RFTS mutations, we opted to mutate mouse DNMT1 proline (P)–496 to tyrosine (Y) that is equivalent to D490/E-P491/Y mutation observed in one family of patients with HSAN1E and tyrosine-500 to

cysteine (C) that is a hotspot mutation for HSAN1E diseases (Fig. 1A) (*30*), respectively. We introduced these mutations into *Dnmt1* coding region by CRISPR-Cas9 technology through injection of appropriate guide RNA (gRNA), donor oligos, and recombinant Cas9 proteins into embryos (*35*). We genotyped the resulting pups by targeted DNA sequencing, which allowed us to determine the identities of wild-type, heterozygous, and homozygous mutant mice accurately (Fig. 1B). Through this approach, we obtained two to three independent heterozygous mutant mice for both *Dnmt1-P496Y* and *Dnmt1-Y500C* mutations but no homozygous mutants for both. For simplicity, we termed the Y500C mutant mice as *Dnmt1-M1* and P496Y mutant mice as *Dnmt1-M2*. Significantly, extensive genotyping analysis revealed that breeding between heterozygous male and female mice generated only wild-type and heterozygous mutant pups and no homozygous offspring for both *Dnmt1-M1* and *Dnmt1-M2* mutants (Fig. 1C). Furthermore, the ratio between wild-type and heterozygous mice is close to 1:2 (Fig. 1C), suggesting that both types of homozygous mutant mice may die during embryogenesis. There was no difference in the growth, general appearance, and life span between wild-type and heterozygous mutant mice (Fig. 1D). As $Dnmt1^{-/-}$ mouse embryos die around embryonic day 9.5 (E9.5) to E10.5 (*27*), we dissected embryos from pregnant female $Dnmt1^{+/M2}$ mutant mice at E11 and E10.5, respectively. We prepared genomic DNA and protein extracts from isolated embryos and performed DNA sequencing analysis for genotyping and Western blotting (WB) analysis for detection of DNMT1 proteins. The representative results in Fig. 1E (top) showed that DNA sequencing identified only wild-type $Dnmt1^{+/+}$ and heterozygous $Dnmt1^{+/M2}$ but no homozygous $Dnmt1^{M2/M2}$ mutants from E11 embryos. WB analysis revealed a clearly reduced level of DNMT1 proteins in the heterozygous mutant embryos (Fig. 1E, bottom). No difference in the level of UHRF1 proteins was detected in WB analysis, suggesting that DNMT1 proteins were specifically down-regulated in $Dnmt1^{+/M2}$ embryos (Fig. 1E, bottom). Notably, the homozygous $Dnmt1^{M2/M2}$ mutant embryos could be identified from the E10.5 embryos (two of seven embryos) (Fig. 1F, top). Furthermore, the $Dnmt1^{M2/M2}$ genotype matched to morphologically defective embryos observed at E10.5 (Fig. 1G). Despite the small sizes of E10.5 $Dnmt1^{M2/M2}$ embryos, we managed to perform WB analysis, and the results in Fig. 1F (bottom) showed that the $Dnmt1^{M2/M2}$ embryos were essentially depleted of DNMT1 proteins, whereas the level of UHRF1 was normal. Together, we have successfully generated two knock-in *Dnmt1* mutant mouse models for human HSAN1E diseases. The heterozygous mutant mice are grossly normal, whereas the homozygous mutant mice die around E10.5 with an apparent deficiency of DNMT1 proteins.

The heterozygous mutant mice have reduced DNMT1 proteins and reduced DNA methylation in various tissues

Our finding that both the *Dnmt1-M1* and *Dnmt1-M2* homozygous mutants are embryonic lethal around E10.5 is reminiscent of the phenotypes of *Dnmt1* knockout mice. This notion is further supported by our observation that the E10.5 $Dnmt1^{M2/M2}$ embryos were deficient of DNMT1 proteins. To investigate this further, we systematically measured the protein and mRNA levels of DNMT1 in various tissues from male littermates of adult wild-type and heterozygous $Dnmt1^{+/M2}$ mice. For comparison of the levels of DNMT1 proteins and mRNA, we also included *Dnmt1* heterozygous ($Dnmt1^{+/-}$) knockout male mice as controls. Representative results in Fig. 2A showed that the levels of DNMT1 proteins in various tissues from $Dnmt1^{+/M2}$ male mice were clearly lower than that from $Dnmt1^{+/+}$ counterparts. Comparison of DNMT1 protein levels among $Dnmt1^{+/+}$, $Dnmt1^{+/-}$, and $Dnmt1^{+/M2}$ revealed that in each tissue, the level of DNMT1 proteins in $Dnmt1^{+/M2}$ is slightly higher than that in $Dnmt1^{+/-}$ but is much lower (approximately half) than that in wild type, except in epencephalon in which the levels of DNMT1 proteins were similar in $Dnmt1^{+/+}$, $Dnmt1^{+/-}$, and $Dnmt1^{+/M2}$ mice. Notably, while *Dnmt1* mRNA level in various $Dnmt1^{+/-}$ mouse tissues (cortex, heart, and lung) is approximately half of that in counterpart tissues from $Dnmt1^{+/+}$ mice, as expected for loss of one *Dnmt1* gene allele, there is no significant difference in Dnmt1 mRNA levels in various tissues between $Dnmt1^{+/M2}$ and $Dnmt1^{+/+}$ mice (Fig. 2B). This effectively excludes the reduced transcription of *Dnmt1* genes as the potential reason for reduced DNMT1 proteins in $Dnmt1^{+/M2}$ mice. Quantitative measurement of DNA methylation in various tissues (cortex, spleen, and lung) revealed a mildly reduced level of DNA methylation in $Dnmt1^{+/M2}$ mice, ranging from a 4.2% reduction in spleen, 4.5% reduction in cortex, to 5.6% reduction in lung in the $Dnmt1^{+/M2}$ mice as compared to the $Dnmt1^{+/+}$ littermates (Fig. 2C). A similar reduction of global DNA methylation was also observed in various tissues from $Dnmt1^{+/-}$ mice (Fig. 2C), consistent with a similar level of reduction of DNMT1 proteins in both $Dnmt1^{+/-}$ and $Dnmt1^{+/M2}$ mice. As an approximately 3% reduction of global DNA methylation was reported for patients with HSAN1E (*36*), we conclude that the $Dnmt1^{+/M2}$ mice exhibit a similar degree of DNA methylation defect as patients with HSAN1E. The same results were observed when female $Dnmt1^{+/+}$, $Dnmt1^{+/-}$, and $Dnmt1^{+/M2}$ mice were analyzed (fig. S1), consistent with the previous observation that the occurrence of HSAN1E diseases is sex independent (*30*, *32*).

To examine whether reduced DNMT1 proteins and impaired DNA methylation are common features of DNMT1 HSAN1E mutations, we also analyzed the levels of DNMT1 proteins; mRNA; and DNA methylation in $Dnmt1^{+/+}$, $Dnmt1^{+/-}$, and $Dnmt1^{+/M1}$ mice essentially as above. As shown in Fig. 2D, we found again in various tissues that the levels of DNMT1 proteins in $Dnmt1^{+/M1}$ mice were reduced by approximately half in comparison to that of $Dnmt1^{+/+}$ mice and are similar to those in $Dnmt1^{+/-}$ mice. No significant difference in the levels of *Dnmt1* mRNA was observed between $Dnmt1^{+/M1}$ and control $Dnmt1^{+/+}$ mice (Fig. 2E). Furthermore, a similar 4 to 5% reduction of global DNA methylation was observed in tissues from $Dnmt1^{+/M1}$ and $Dnmt1^{+/-}$ as compared to that in $Dnmt1^{+/+}$ mice (Fig. 2F). Last, a similar reduced level of DNMT1 proteins and DNA methylation was also observed in various tissues from female $Dnmt1^{+/M1}$ mice (fig. S2).

Together, both the P496Y and Y500C mutations in the RFTS domain of mouse DNMT1 lead to reduced levels of DNMT1 proteins, but not mRNAs, in most, if not all, mouse tissues that we have analyzed. Furthermore, the reduced DNMT1 proteins are likely causal to the reduced global DNA methylation in both heterozygous mutant mice because a similar level of reduction in DNA methylation is observed in $Dnmt1^{+/-}$ mice. A similar degree of global DNA methylation reduction in patients with HSAN1E and *Dnmt1-M1* and *Dnmt1-M2* mice underscores a conserved mechanism as to how the DNMT1 mutations affect DNA methylation and underpins *Dnmt1-M1* and *Dnmt1-M2* mice as the models for HSAN1E diseases.

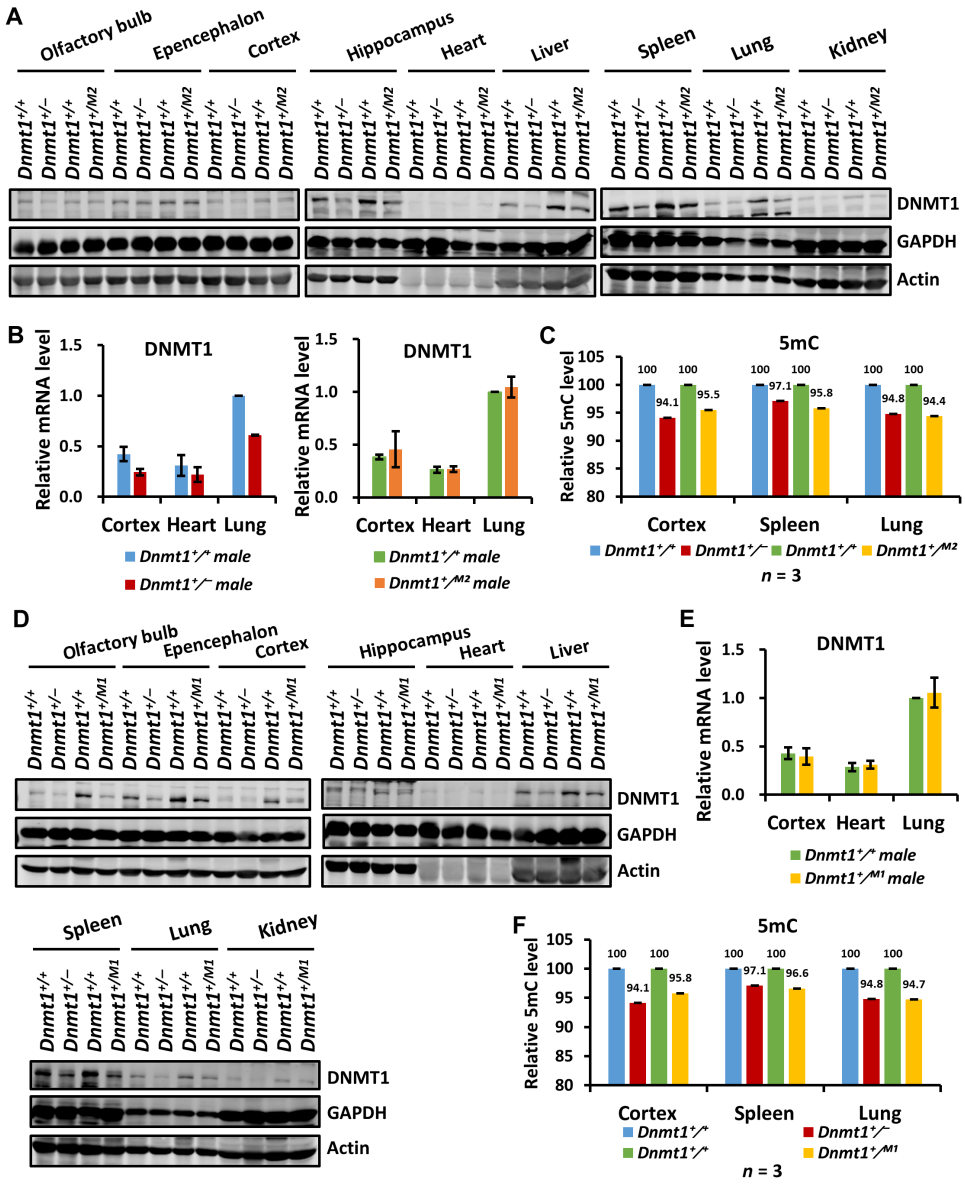

Fig. 2. Both heterozygous knock-in mutant mice show reduction of DNMT1 proteins and DNA methylation in various tissues. (**A**) WB analysis showing a reduced level of DNMT1 proteins in *Dnmt1*$^{+/M2}$ in comparison to *Dnmt1*$^{+/+}$ for all tissues analyzed except epencephalon. GAPDH, glyceraldehyde-3-phosphate dehydrogenase. (**B**) Reverse transcription polymerase chain reaction (RT-PCR) analysis of the levels of Dnmt1 mRNA in the tissues of *Dnmt1*$^{+/+}$ and *Dnmt1*$^{+/M2}$ mice. (**C**) Levels of DNA methylation in the tissues of *Dnmt1*$^{+/+}$ and *Dnmt1*$^{+/M2}$ mice determined by high-performance liquid chromatography (HPLC). 5mC, 5-methylcytosine. (**D**) WB analysis showing a reduced level of DNMT1 proteins in *Dnmt1*$^{+/M1}$ in comparison to *Dnmt1*$^{+/+}$ for all tissues analyzed. (**E**) RT-PCR analysis of the levels of Dnmt1 mRNA in the tissues of *Dnmt1*$^{+/+}$ and *Dnmt1*$^{+/M1}$ mice. (**F**) Levels of DNA methylation in the tissues of *Dnmt1*$^{+/+}$ and *Dnmt1*$^{+/M1}$ mice determined by HPLC.

Impaired neurogenesis and cognitive function in *Dnmt1* heterozygous mutant mice

We next examined whether the *Dnmt1-M1* and *Dnmt1-M2* mice exhibit neurodegenerative phenotypes as defined in patients with HSAN1E. We first examined the effects of *Dnmt1* mutation on neurogenesis in vitro by analyzing the adult neural stem cells (aNSCs) isolated from the brain of adult *Dnmt1*$^{+/+}$ and *Dnmt1*$^{+/M2}$ mice, respectively. 5-Bromo-2′-deoxyuridine (BrdU) incorporation assay was performed to analyze the proliferative capability of aNSCs. Double immunostaining of BrdU and aNSCs marker Sox2 (SRY-box transcription factor 2) allowed the identification of proliferative aNSCs, and quantification results showed that the percentage of proliferating BrdU-positive (BrdU^{+}) cells was significantly lower in *Dnmt1*$^{+/M2}$ aNSCs compared to the *Dnmt1*$^{+/+}$ cells (Fig. 3, A and B). We induced aNSCs to differentiate and observed that *Dnmt1*$^{+/M2}$ aNSCs produced fewer class III beta-tubulin (Tuj1^{+}) neurons, but more glial fibrillary acidic protein–positive (Gfap^{+}) astrocytes, compared to *Dnmt1*$^{+/+}$ aNSCs (Fig. 3, C to E).

To determine the effects of *Dnmt1* mutation on neurogenesis in vivo, *Dnmt1*$^{+/+}$ and *Dnmt1*$^{+/M2}$ mice were administrated with BrdU (50 mg/kg, intraperitoneally) using a protocol illustrated in fig. S3A to mark the proliferative aNSCs. We sacrificed the mice

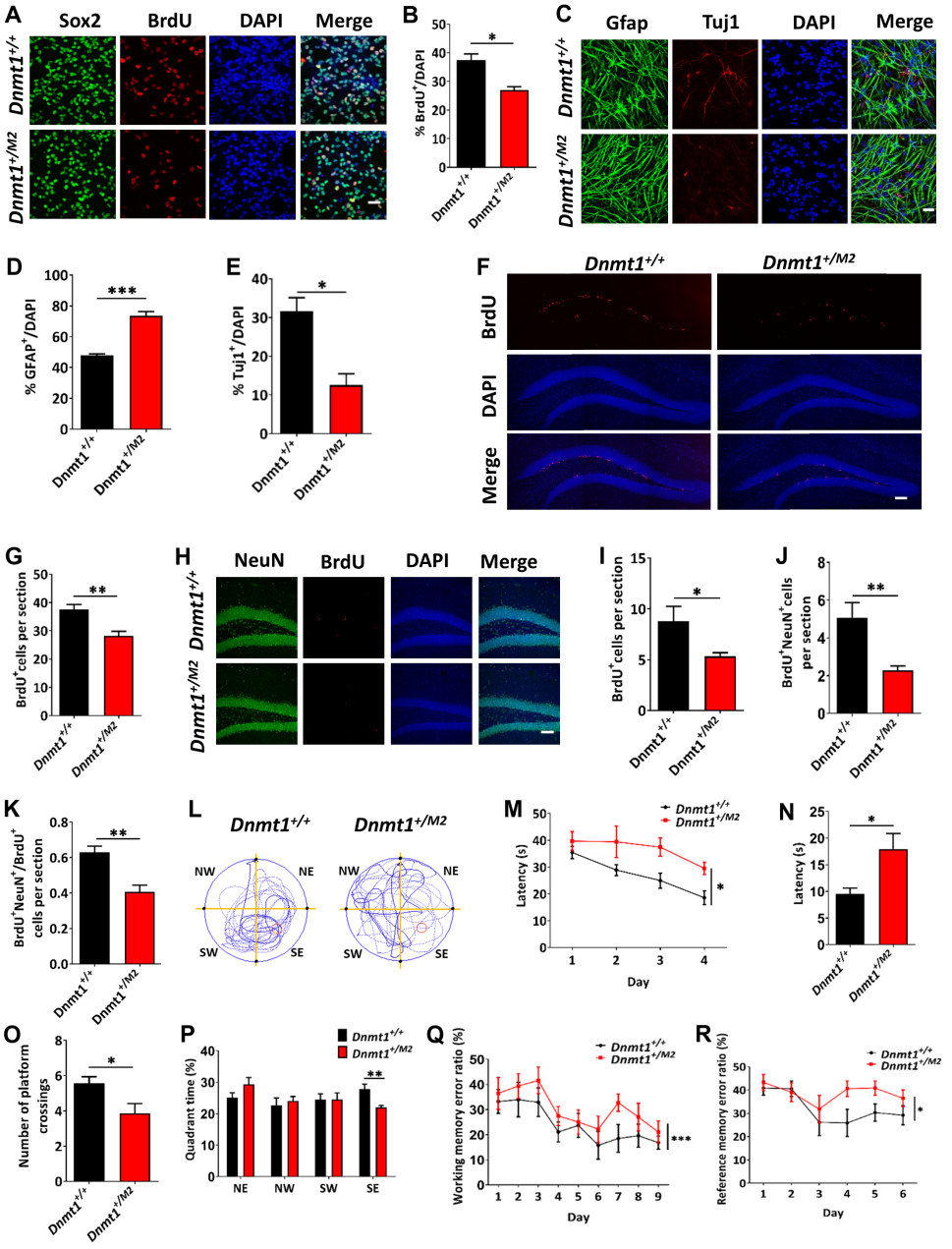

Fig. 3. Impaired learning and memory of adult *Dnmt1* mutant mice. (**A**) BrdU immunofluorescence staining of aNSCs. DAPI, 4′,6-diamidino-2-phenylindole. (**B**) Quantification results of BrdU$^+$-labeled *Dnmt1*$^{+/+}$ and *Dnmt1*$^{+/M2}$ aNSCs. $n = 3$. (**C**) Gfap and Tuj1 immunofluorescence staining of aNSCs. (**D** and **E**) Quantification of the percentage of GFAP$^+$ (D) and Tuj1$^+$ (E) cells from differentiated *Dnmt1*$^{+/+}$ and *Dnmt1*$^{+/M2}$ aNSCs. $n = 3$. (**F**) BrdU immunofluorescence staining of the hippocampus from *Dnmt1*$^{+/+}$ and *Dnmt1*$^{+/M2}$ mice. (**G**) Quantification results of BrdU$^+$ cells. *Dnmt1*$^{+/+}$: $n = 4$; *Dnmt1*$^{+/M2}$: $n = 5$. (**H**) BrdU and NeuN immunofluorescence staining of the hippocampus. Scale bar, 100 μm. (**I** to **K**) Quantification results of BrdU$^+$ (I) and BrdU$^+$NeuN$^+$ (J) and the percentage of BrdU$^+$NeuN$^+$/BrdU$^+$ (K) cells. *Dnmt1*$^{+/+}$: $n = 4$; *Dnmt1*$^{+/M2}$: $n = 5$. (**L**) Swimming path of mice in Morris water maze. (**M**) Average time to reach the platform during the training period of Morris water maze. $n = 7$. (**N** to **P**) Average time to find the platform (N), numbers of crossing platform (O), and time in target quadrant (P). $n = 7$. (**Q**) Mouse working memory error rate during the experiment. $n = 9$. (**R**) Mouse reference memory error rate during the experiment. $n = 9$. Unpaired Student's *t* test (B, D, E, G, I, J, K, N, O, and P) or paired Student's *t* test (M, Q, and R) was used for statistical analysis. $^*P < 0.05$, $^{**}P < 0.01$, and $^{***}P < 0.001$. All scale bars, 100 μm.

and performed BrdU immunostaining 4 hours after final BrdU administration to determine the level of proliferative aNSCs and newborn immature neurons. We observed that the numbers of BrdU$^+$ aNSCs and newborn immature neurons doublecortin (DCX$^+$) were significantly decreased in *Dnmt1*$^{+/M2}$ mice compared to *Dnmt1*$^{+/+}$ mice (Fig. 3, F and G, and fig. S3, C and D). To examine whether the mutation affects the neuronal differentiation, we used a protocol shown in fig. S3B that NSCs were pulse labeled by BrdU. We then examined the number of BrdU$^+$ differentiated neuronal cells 4 weeks after final BrdU administration. We found that the numbers of BrdU$^+$ cells and numbers of BrdU$^+$NeuN$^+$ cells were both significantly decreased in *Dnmt1*$^{+/M2}$ mice compared to *Dnmt1*$^{+/+}$ mice (Fig. 3, H to K).

We also examined whether there is increased cell death in mutant mice by TUNEL (terminal deoxynucleotidyl transferase–mediated deoxyuridine triphosphate nick end labeling) assay of hippocampal slices. The representative results in fig. S4 show an increased level of TUNEL-positive cells in mutant hippocampal slices versus control, although the overall level of TUNEL-positive cells in mutants is still very low. Collectively, these results suggest that *Dnmt1* mutation leads to the decreased proliferation, aberrant differentiation of aNSCs in vitro and in vivo, and a slight increased cell death.

Given the important roles of adult neurogenesis in learning and memory (*37*–*39*) and in neuropathy symptoms in patients with HSAN1E (*30*, *32*), we next analyzed the effects of *Dnmt1* mutation on the cognitive function of mice. Morris water maze test showed that $Dnmt1^{+/M2}$ mice displayed longer time to find the platform during the training period (Fig. 3, L and M). The probe trial tests performed 24 hours after the training revealed that $Dnmt1^{+/M2}$ mice displayed longer latency, fewer numbers of platform crossing, and less time spent in target quadrant while there is no difference in swimming speed compared to $Dnmt1^{+/+}$ mice (Fig. 3, N to P, and fig. S3E). We also carried out a radial eight-arm maze test (fig. S3F) and observed that $Dnmt1^{+/M2}$ mice showed higher working and reference memory error ratios relative to $Dnmt1^{+/+}$ mice (Fig. 3, Q to R). In pattern separation test, $Dnmt1^{+/M2}$ mice showed no preference in exploring congruent and incongruent objects compared to $Dnmt1^{+/+}$ mice, which spent more time exploring the incongruent object during the test phase (fig. S3, G to J). Together, these results suggest that $Dnmt1^{+/M2}$ mice have impaired cognitive function.

Endogenous mutant DNMT1 proteins in mouse embryonic stem cells is unstable

Having established that the mutant *Dnmt1* mice exhibit impaired neurogenesis and cognitive function, we next investigated how the RFTS P496Y and Y500C mutations result in reduced DNMT1 proteins but not mRNA, as this is most likely causal to the human disease and cognitive phenotype in mice. To this end, we derived wild-type, heterozygous, and homozygous mutant mouse embryonic stem (mES) cells from blastocysts (Fig. 4A). Through extensive efforts, we managed to establish $Dnmt1^{+/+}$, $Dnmt1^{+/M1}$, and $Dnmt1^{M1/M1}$ mES cell lines from the same batch of blastocysts. By the same approach, we also successfully derived $Dnmt1^{+/+}$ and $Dnmt1^{+/M2}$ mES cell lines, although genotyping identified no $Dnmt1^{M2/M2}$ ES cell line. Subsequent WB analysis revealed a progressively reduced level of DNMT1 proteins in $Dnmt1^{+/M1}$ and $Dnmt1^{M1/M1}$ mES cells as compared to $Dnmt1^{+/+}$ mES cells (Fig. 4B). The reduced DNMT1 proteins in $Dnmt1^{+/M1}$ and $Dnmt1^{M1/M1}$ mES cells are not due to change in transcription, as the levels of *Dnmt1* mRNA were similar in all three types of mES cells (Fig. 4C). Quantitative measurement of the levels of global DNA methylation by high-performance liquid chromatography (HPLC) revealed a modest reduction of DNA methylation in $Dnmt1^{+/M1}$ mES cells and a much more severe reduction of DNA methylation in the $Dnmt1^{M1/M1}$ mES cells (Fig. 4D). Similar analysis also confirmed a reduced level of DNMT1 proteins but not mRNA in $Dnmt1^{+/M2}$ mES cells as compared to $Dnmt1^{+/+}$ mES cells (fig. S5, A and B). In addition, a reduced level of DNA methylation was also observed in $Dnmt1^{+/M2}$ mES cells (fig. S5C). Together, these results reveal a causal relationship between reduction of DNMT1 proteins and impairment of DNA methylation.

Previous studies suggested that the RFTS mutations in DNMT1 lead to protein misfolding and to increased sensitivity to proteasome degradation (*30*, *32*). With the availability of $Dnmt1^{+/+}$, $Dnmt1^{+/M1}$, and $Dnmt1^{M1/M1}$ mES cell lines, we next examined whether the RFTS mutation indeed impaired DNMT1 protein stability in mES cells. Standard protein stability assay with inhibition of protein synthesis by cycloheximide revealed a marked reduction of DNMT1 protein stability in $Dnmt1^{M1/M1}$ mES cells, with half-life reduced from ~12 hours in $Dnmt1^{+/+}$ to ~4 hours in $Dnmt1^{M1/M1}$ ES cells (Fig. 4E). The half-life of DNMT1 in $Dnmt1^{+/M1}$ mES cells was similar to that in $Dnmt1^{+/+}$, most likely because the majority of the DNMT1 proteins in $Dnmt1^{+/M1}$ cells were actually wild-type DNMT1. Notably, by extensive experiments, we observed that addition of MG132 (*N*-carbobenzyloxy-L-leucyl-L-leucyl-L-leucinal), a potent inhibitor of proteasome degradation, could not rescue the level of mutant DNMT1 proteins, whereas it markedly elevated the levels of p53 (Fig. 4F). Similarly, we found that addition of chloroquine (CQ), an inhibitor of lysosome-mediated autophagy degradation, also failed to rescue mutant DNMT1 protein stability either when used alone (Fig. 4G) or together with MG132 (Fig. 4H). Similar results were observed for $Dnmt1^{+/M2}$ mES cells (fig. S5, D to G). We thus conclude that although the mutant DNMT1 proteins are indeed unstable as compared to the wild-type DNMT1 proteins, they are not more sensitive than the wild-type proteins to degradation by either proteasome or lysosomes.

The endogenous mutant DNMT1 proteins are most likely cleaved at the RFTS region by a novel proteinase

Because we found no evidence that the mutant DNMT1 proteins were preferentially degraded by proteasome or autophagy, we explored whether the mutant DNMT1 proteins might be unstable because of degradation by proteinase cleavage. To this end, we immunoprecipitated DNMT1 proteins from $Dnmt1^{+/+}$ and $Dnmt1^{M1/M1}$ mES cells by an antibody specific for N-terminal region of DNMT1 and analyzed the isolated DNMT1 proteins by WB. As shown in Fig. 5A, WB analysis detected a truncated DNMT1 protein with a molecular mass approximately 75 to 80 kDa from $Dnmt1^{M1/M1}$ but not from $Dnmt1^{+/+}$ mES cells. In addition, a similar truncated DNMT1 protein was detected in $Dnmt1^{+/M2}$ mES cells (Fig. 5B), indicating that both DNMT1-M1 and DNMT1-M2 mutant proteins could give rise to truncated proteins with a similar size. Although many DNMT1 bands with molecular weights smaller than full-length protein were detected in our immunoprecipitation (IP)–WB analysis, they most likely represented the endogenous degraded DNMT1 and/or DNMT1 variants, as the DNMT1 antibody used for IP-WB is highly specific (*25*). The detection of this unique 75- to 80-kDa truncated DNMT1 protein from both DNMT1 mutant proteins suggested that the mutant DNMT1 is likely cleaved at the RFTS region by a specific proteinase. This internal cleavage not only would inactivate DNMT1 but also could lead to further degradation of truncated DNMT1, thus at least partially explaining the reduced levels of DNMT1 proteins in homozygous embryos, mutant ES cells, and heterozygous mice.

The RFTS mutant DNMT1 proteins show aberrant nucleolar localization

As RFTS mutations have been reported to cause DNMT1 aggregates in cytoplasm (*32*), we next examined the subcellular localization of mutant DNMT1 proteins in $Dnmt1^{M1/M1}$ mES cells by confocal microscope. As expected, DNMT1 in interphase $Dnmt1^{+/+}$ mES cells was observed as a typical diffuse nuclear staining pattern (Fig. 5C, top).

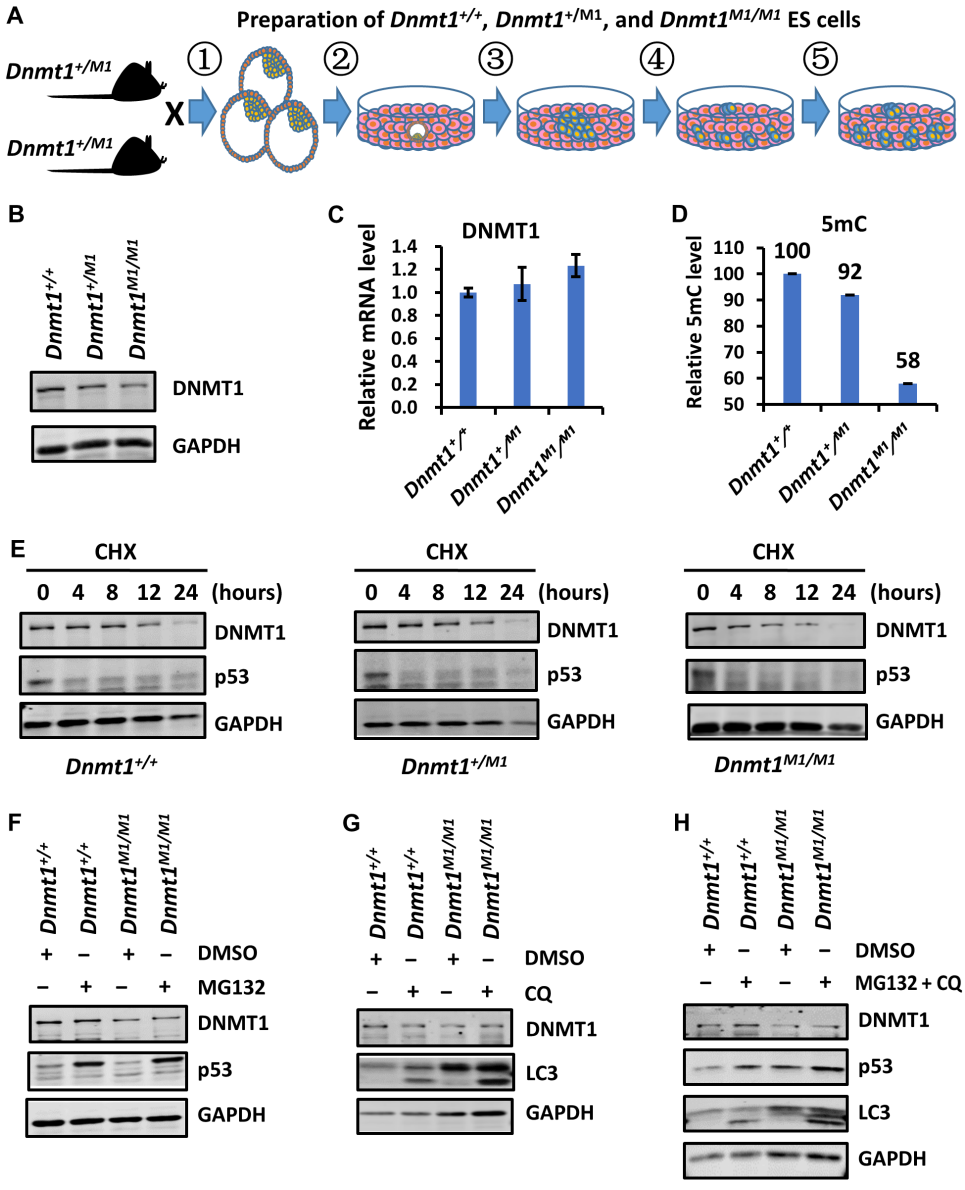

Fig. 4. Mutant DNMT1 proteins were unstable in mES cells. (**A**) Schematic diagram illustrating the protocol for deriving mES cells from E3.5 blastocysts. (**B**) WB analysis showing the levels of DNMT1 proteins in *Dnmt1*$^{+/+}$, *Dnmt1*$^{+/M1}$, and *Dnmt1*$^{M1/M1}$ mES cells. (**C**) RT-PCR analysis of the levels of Dnmt1 mRNA in different mES cells. (**D**) The levels of DNA methylation in *Dnmt1*$^{+/+}$, *Dnmt1*$^{+/M1}$, and *Dnmt1*$^{M1/M1}$ mES cells as determined by HPLC. (**E**) Stability of DNMT1 proteins in different mES cells. The mES cells were treated with cycloheximide (CHX; 100 μg/ml) for various times as indicated. The cells were collected and analyzed by WB using antibodies as indicated. As a control, p53 was rapidly degraded upon cycloheximide treatment. (**F**) WB analysis showing that MG132 treatment could not stabilize DNMT1 in *Dnmt1*$^{M1/M1}$ mES cells. MG132, 10 μM for 12 hours. (**G**) WB analysis showing that CQ treatment could not stabilize DNMT1 in *Dnmt1*$^{M1/M1}$ mES cells. CQ, 1 μM for 12 hours. Note that LC3 level increased upon CQ treatment. (**H**) WB analysis showing that combined CQ and MG132 treatment could not stabilize DNMT1 in *Dnmt1*$^{M1/M1}$ mES cells. CQ, 1 μM; MG132, 10 μM. Cells were treated for 12 hours.

However, DNMT1 in the vast majority of *Dnmt1*$^{M1/M1}$ mES cells was seen as one or a few nuclear foci (Fig. 5C, bottom, a large foci indicated by a white arrow). Notably, the nuclear DNMT1 foci in *Dnmt1*$^{M1/M1}$ mES cells were found to colocalize with upstream binding factor (UBF), a nucleolar resident protein (Fig. 5D), indicating that the mutant DNMT1 proteins were mislocalized to the nucleolus. Note that these DNMT1 nucleolar foci were also observed in a small percentage of *Dnmt1*$^{+/M1}$ mES cells (3 of 77 cells) but not in *Dnmt1*$^{+/+}$ mES cells (Fig. 5D). Similarly, we observed DNMT1 nucleolar localization in a small percentage of *Dnmt1*$^{+/M2}$ mES cells (Fig. 5E, top). DNMT1 nucleolar localization was observed in ~15% of mouse embryonic fibroblast (MEF) cells derived from *Dnmt1*$^{+/M2}$ mice (Fig. 5E, bottom), suggesting that the extents of nucleolar mislocalization of mutant DNMT1 proteins may vary by cell types. Furthermore, such mislocalization of mutant DNMT1 was also observed in primary NSCs derived from *Dnmt1*$^{+/M2}$ mice (Fig. 5F). The low rate of DNMT1 nucleolar–positive cells detected in heterozygous mutant ES, MEFs, and NSCs is likely explained, as

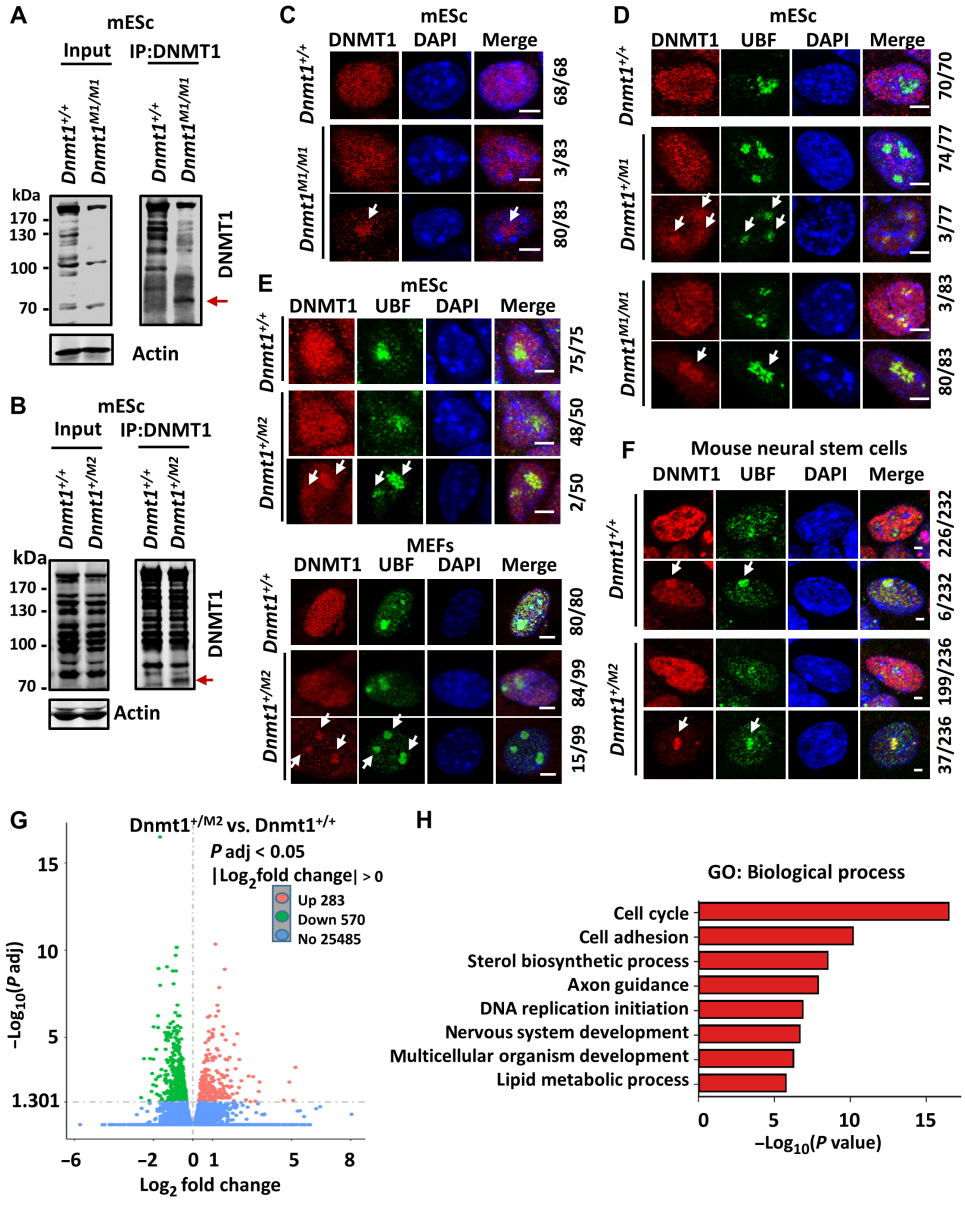

Fig. 5. Novel proteolytic cleavage and nucleolus mislocalization of mutant DNMT1 proteins and aberrant gene expression in *Dnmt1*$^{+/M2}$ NSCs. (**A** and **B**) IP-WB analysis showing the existence of a specific truncated DNMT1 protein (indicated by a red arrow) in *Dnmt1*$^{M1/M1}$ (A) and *Dnmt1*$^{+/M2}$ (B) mES cells. (**C**) Immunofluorescence staining showing the difference in subcellular localization of wild-type and mutant DNMT1 proteins. Scale bars, 5 μm. The numbers on the right indicate the type of cells out of total counted cells. (**D**) Double immunofluorescence staining of DNMT1 and upstream binding factor (UBF) in *Dnmt1*$^{+/+}$, *Dnmt1*$^{+/M1}$, and *Dnmt1*$^{M1/M1}$ mES cells. White arrows indicate the colocalization of DNMT1 and UBF. Scale bars, 5 μm. (**E**) Double immunofluorescence showing DNMT1 and UBF colocalization in a small percentage of *Dnmt1*$^{+/M2}$ mES cells (top; scale bars, 5 μm) and mouse embryonic fibroblasts (MEFs) (bottom; scale bars, 20 μm). (**F**) Double immunofluorescence staining showing DNMT1 and UBF colocalization in approximately 15.6% of *Dnmt1*$^{+/M2}$ versus 2.5% of *Dnmt1*$^{+/+}$ aNSCs. Scale bars, 5 μm. (**G**) Volcano plot showing differentially expressed genes between control and *Dnmt1*$^{+/M2}$ aNSCs. RNA sequencing (RNA-seq) analyses were performed in triplicates of biological repeats. (**H**) Most significant changed gene ontology (GO) terms in *Dnmt1*$^{+/M2}$ aNSCs compared with *Dnmt1*$^{+/+}$ aNSCs. WT: $n = 3$; Het: $n = 3$.

the majority of DNMT1 proteins in these cells are actually wild-type DNMT1 proteins. Together, these data indicate that nucleolar mislocalization is a common feature of the RFTS mutant DNMT1.

Aberrant gene expression in adult Dnmt1$^{+/M2}$ NSCs

To investigate how DNMT1 mutation affects gene expression in mice, we carried out RNA sequencing (RNA-seq) analysis of aNSCs from three pairs of wild-type and Dnmt1$^{+/M2}$ littermates. This effort collectively identified 283 up-regulated and 570 down-regulated genes in Dnmt1$^{+/M2}$ NSCs, with *P*adj < 0.05 as a cutoff (Fig. 5G). Gene ontology analysis of these differentially expressed genes revealed significant enrichment for genes involved in cell cycle, cell adhesion, axon guidance, and nervous system development, consistent with our observed proliferation and differentiation defects of NSCs and impaired learning and memory of the mutant mice (Fig. 5H).

The nucleolar mislocalized mutant DNMT1 proteins are a truncated form of DNMT1

Given our observation that the mutant DNMT1 proteins give rise to a truncated form of DNMT1, we wish to determine whether the nucleolar localized DNMT1 represents the full-length mutant DNMT1 or the truncated DNMT1 proteins. We surmised that the nucleolar localization is likely a feature of truncated mutant DNMT1 proteins because this was not observed in previous studies using ectopically expressed DNMT1 mutants (*30*, *32*). Nevertheless, we examined the subcellular localization and protein stability of DNMT1-M1 and DNMT1-M2 mutants in the form of FLAG-tagged fusions in HeLa and NIH3T3 cells. We found that ectopically expressed FLAG-DNMT1-M1 and FLAG-DNMT1-M2 displayed a typical diffuse nuclear staining in interphase HeLa cells (fig. S6A). In NIH3T3 cells, both wild-type and DNMT1-M1 and M2 mutants exhibited a diffuse nuclear staining in interphase cells and a typical foci pattern that overlapped with the 5-ethynyl-2′-deoxyuridine (EdU) foci in S phase cells (fig. S6B). In these experiments, we found no evidence for mutant DNMT1 nucleolar or cytoplasmic localization (fig. S6, A and B). Furthermore, FLAG-DNMT1-M1 and FLAG-DNMT1-M2 were primarily detected as full-length proteins and as stable as the wild-type DNMT1 when ectopically expressed in HeLa cells (fig. S6C). IP followed by WB analysis revealed that the mutant DNMT1 proteins had no defect in interaction with UHRF1 (fig. S6D). The discrepancy in subcellular localization and protein stability between our current and previous studies could be due to a difference in protein tag, with green fluorescent protein (GFP) used in the previous studies (*30*, *32*) and with FLAG used here. Together, these results indicate that in the absence of obvious proteinase cleavage, the mutant DNMT1 proteins display normal subcellular localization and are as stable as wild-type DNMT1.

To test directly whether truncated DNMT1 would localize to the nucleolus, we generated a series of DNMT1 constructs expressing various length of DNMT1 N-terminal domains (Fig. 6A, top). We found that the N-terminal amino acid 1 to 501 fragment has a similar size as the truncated DNMT1 proteins detected in both *Dnmt1*$^{M1/M1}$ and *Dnmt1*$^{+/M2}$ mES cells (Fig. 6A, bottom), suggesting that proteolytic cleavage of mutant DNMT1 proteins likely occurs in the vicinity of amino acid 501 within the RFTS region. We thus carried out immunofluorescent staining analysis of FLAG-DNMT1 (amino acids 1 to 501) and additional truncated DNMT1 proteins in HeLa cells. As shown in Fig. 6B, whereas both wild-type and DNMT1-M1 mutant proteins exhibited a typical nuclear localization, the DNMT1 (amino acids 1 to 501) displayed both weak and strong nucleolar localization. Similar results were observed for additional truncated DNMT1 constructs, suggesting that nucleolar mislocalization is a shared property of truncated DNMT1 proteins. As no mislocalization for full-length DNMT1-M1 and DNMT1-M2 mutants was observed in HeLa cells, we suggest that HeLa cells may lack the proteinase(s) required for cleavage of mutant DNMT1 proteins (see next). Together, we conclude that the nucleolar localized DNMT1 proteins observed in both hetero- and homozygous *Dnmt1* mutant cells are most likely the truncated mutant DNMT1.

The DNMT1-M1 mutant human glioma cells generated by base editing are defective in cell proliferation and show DNMT1 nucleolar mislocalization

Thus far, our studies with mutant mice and mouse cells point to proteinase cleavage of mutant DNMT1 as the potential mechanism for functional defect of DNMT1 proteins in HSAN1E neurodegenerative diseases. To validate our findings in human neuronal cells, we attempted to generate DNMT1-M1 mutant cell lines from HS683 glioma cells by converting nucleotide 1484A in the DNMT1 coding region to G (corresponding to Y495C mutation) through base editing technology using ABEmax (Fig. 6C). Targeted sequencing of DNMT1 genomic DNA from ABEmax-edited cell mixtures revealed that ~10 to 15% of DNMT1 contained A1484 to G mutation (Fig. 6D). We then attempted to isolate mutated clones through single-cell sorting. We observed two types of single-cell clones, one with normal rate of proliferation and the other poor in proliferation. The latter type ceased to proliferate after reaching ~60 cells. We performed immunofluorescent staining to analyze DNMT1 subcellular localization in both types of clones. A regular diffuse nuclear staining was observed in most cells in the normal proliferating clones (61 of 61 clones) (Fig. 6E). However, for clones with poor proliferation (7 of 7), we observed weaker DNMT1 staining and colocalization of DNMT1 with UBF in foci, indicating that DNMT1 was mislocalized to the nucleolus in these cells. We could not perform genomic DNA sequencing to precisely determine the genotype of these poor proliferating clones owing to insufficient quantity of cells; however, these clones most likely were homozygous DNMT1-M1 cells based on the facts that DNMT1 was mislocalized to the nucleolus and that these cells were poor in proliferation. DNMT1 is known to be required for proliferation of HCT116 cells (*40*, *41*) and therefore also may be required for appropriate cell proliferation of HS683 glioma cells.

Mutant DNMT1 proteins without proteolytic cleavage is essentially normal in subcellular localization, protein stability, and enzymatic activity

Although we failed to obtain long-term viable homozygous DNMT1-M1 mutant cells from HS683 glioma cells, we successfully isolated viable homozygous DNMT1-M1 mutant clones from HeLa cells through a base editing approach as above (Fig. 7, A to C). On the basis of the representative DNA sequencing profiles in Fig. 7C, we assigned homozygous DNMT1-M1 clones as those with no residual wild-type A1484 signal and heterozygous clones as those with approximately 50:50 ratio of A and G at DNMT1 nucleotide 1484. Through this rigid genotyping method, we obtained multiple wild-type, heterozygous, and homozygous DNMT1-M1(Y495C) mutant clones. WB analysis of representative clones revealed a similar level of DNMT1 proteins in wild-type, heterozygous, and homozygous DNMT1-M1 clones (Fig. 7D). Furthermore, protein stability assay revealed that the DNMT1 proteins in homozygous *DNMT1*$^{M1/M1}$ HeLa cells were as stable as those in wild-type *DNMT1*$^{+/+}$ cells (Fig. 7E), and this conclusion is further confirmed by experiments with addition of proteasome inhibitor MG132 (Fig. 7F). Thus, in contrast to a reduced stability of DNMT1-M1 mutant proteins in *Dnmt1*$^{M1/M1}$ mES cells, the same mutation did not reduce the protein stability in HeLa cells. Furthermore, in contrast to nucleolar mislocalization in *Dnmt1*$^{M1/M1}$ mES cells, the DNMT1-M1 proteins in HeLa cells exhibited a normal diffuse nuclear staining (Fig. 7G). In addition, in contrast to a severe reduction of global DNA methylation in *Dnmt1*$^{M1/M1}$ mES cells, the global levels of DNA methylation were reduced only slightly in various *DNMT1*$^{M1/M1}$ HeLa clones that we have analyzed (Fig. 7H). Unlike the case in *Dnmt1*$^{M1/M1}$ mES cells, we failed to detect the presence of truncated 75- to 80-kDa DNMT1 proteins in *DNMT1*$^{M1/M1}$ HeLa cells by IP-WB analysis (fig. S7). The lack of truncated DNMT1 proteins in *DNMT1*$^{M1/M1}$ HeLa cells

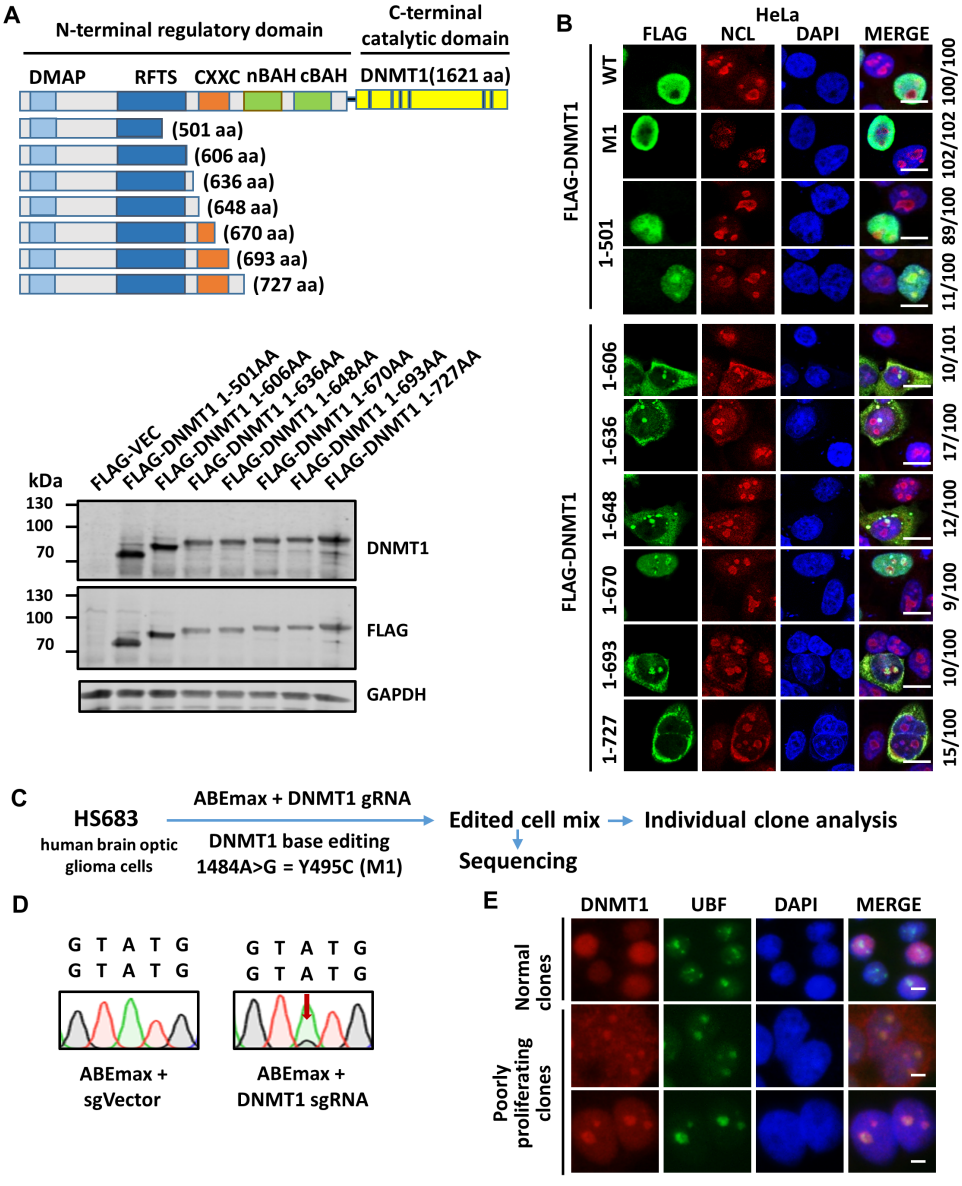

Fig. 6. Nucleolus mislocalization of DNMT1 truncated mutants and DNMT1-M1 mutant proteins generated by base editing in human glioma cells. (**A**) Diagrams on the top panel illustrating a series of truncated DNMT1 mutant proteins. Also shown are WB analyses of the truncated DNMT1 in HeLa cells. Note that the size of DNMT1 (amino acids 1 to 501) is similar to the size of truncated DNMT1 proteins detected in mutant mES cells. (**B**) Double immunofluorescence staining showing colocalization of truncated DNMT1 (amino acids 1 to 501) and other mutants with nucleolin (NCL) in HeLa cells. No such colocalization was observed for wild-type DNMT1 and DNMT1-M1 mutant. Scale bars, 20 μm. (**C**) Diagram illustrating scheme of generating DNMT1 Y495C M1 mutation in human glioma HS683 cells by mutation of DNMT1 1484A>G through base editing. (**D**) HS683 cells edited with ABEmax plus control single gRNA (sgRNA) vector or plasmid expressing specific DNMT1-M1 sgRNA were collected and subjected to DNA sequencing for DNMT1 1484A>G mutation. Approximately 10 to 15% DNA molecules contained 1484G residue. (**E**) Double immunofluorescence staining showing typical DNMT1 diffuse nuclear staining pattern in normal proliferating HS683 clones (61 of total 68) and DNMT1 nucleolus localization in poorly proliferating HS683 clones (7 of total 68). Scale bars, 5 μm.

is consistent with the lack of DNMT1 nucleolar localization in these cells. Together, these results indicate that without proteinase cleavage, the mutant DNMT1 proteins are essentially normal in subcellular localization, protein stability, and DNA methyltransferase activity.

DISCUSSION

In this study, we successfully generated two *Dnmt1* knock-in mouse models for human HSAN1E diseases. Similar phenotypes are observed for both models, although the subtle phenotypic difference between two *Dnmt1* mutation models, if it existed, remains to be investigated. Both homozygous *Dnmt1* mutants are embryonic lethal, whereas the heterozygous mutants are viable and normal in growth and gross appearance. However, the heterozygous mutants do exhibit reduced neuronal proliferation and differentiation ability and impaired learning and memory, which, to some extent, manifest symptoms observed in human patients with HSAN1E (*30*, *32*). Notably, our cellular and biochemical studies point to specific proteinase cleavage

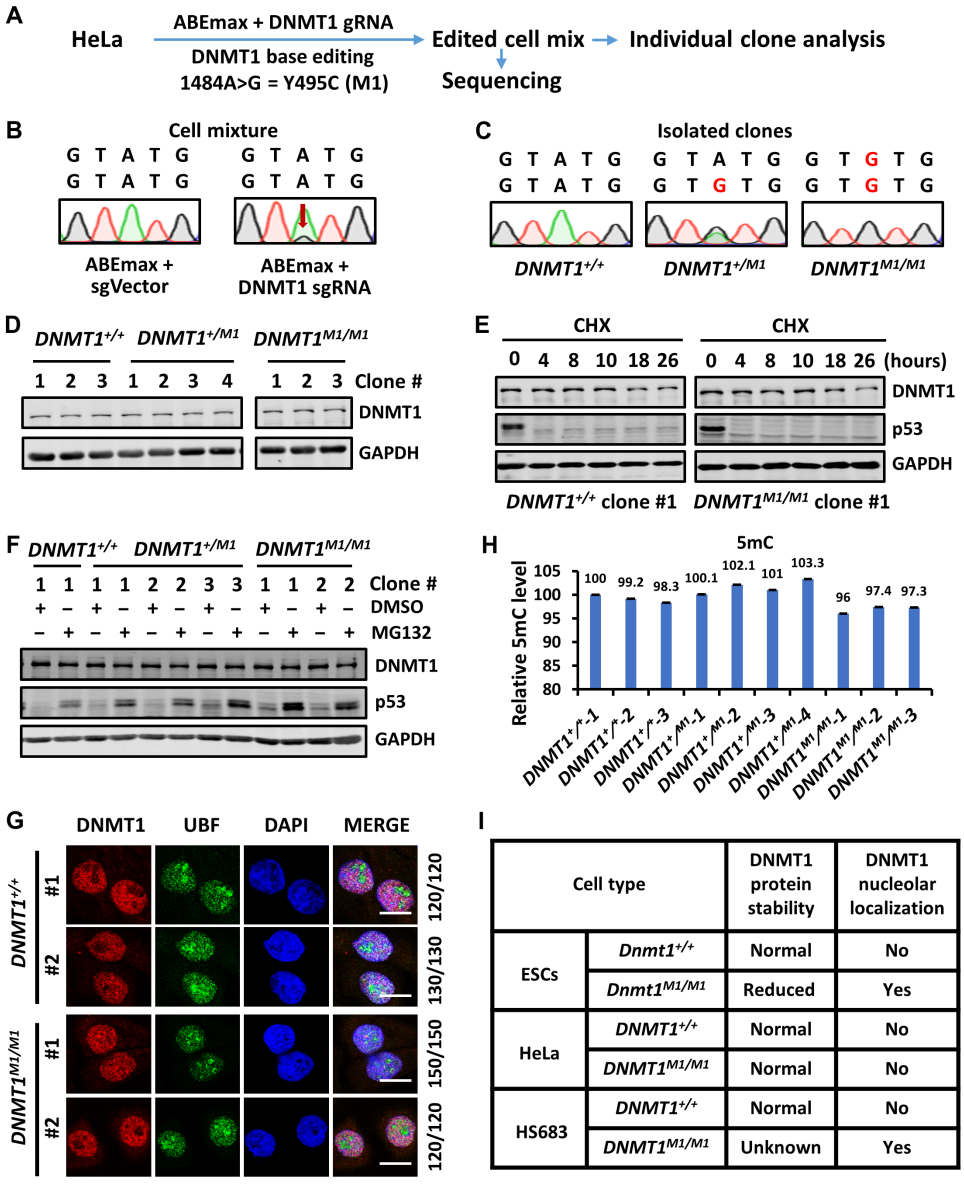

I

Cell type		DNMT1 protein stability	DNMT1 nucleolar localization
ESCs	*Dnmt1*$^{+/+}$	Normal	No
	Dnmt1$^{M1/M1}$	Reduced	Yes
HeLa	*DNMT1*$^{+/+}$	Normal	No
	DNMT1$^{M1/M1}$	Normal	No
HS683	*DNMT1*$^{+/+}$	Normal	No
	DNMT1$^{M1/M1}$	Unknown	Yes

Fig. 7. The DNMT1-M1 mutant proteins in HeLa cells are intact, stable, functionally active, and display no nucleolus localization. (**A**) Diagram illustrating scheme of generating Y495C M1 mutation in DNMT1 in HeLa cells by mutation of DNMT1 1484A>G through base editing. (**B** and **C**) DNA sequencing analysis of cell mixture (B) and isolated clones derived from single cells (C). DNA sequencing unambiguously identified wild-type, heterozygous, and homozygous HeLa cell lines. (**D**) WB analysis showing the levels of DNMT1 proteins in wild-type, heterozygous, and homozygous DNMT1-M1 HeLa cell lines. (**E**) Comparison of DNMT1 protein stability in wild-type and homozygous DNMT1-M1 HeLa cell lines. (**F**) WB analysis showing that addition of MG132 did not significantly elevate the level of DNMT1 proteins in wild-type, heterozygous, and homozygous DNMT1-M1 HeLa cell lines. DMSO, dimethyl sulfoxide. (**G**) Double immunofluorescence staining showing the localization of DNMT1 and UBF in wild-type and homozygous DNMT1-M1 HeLa cell lines. Scale bars, 20 μm. (**H**) The levels of DNA methylation in wild-type, heterozygous, and homozygous DNMT1-M1 HeLa cell lines determined by HPLC. (**I**) Summary of protein stability and localization of DNMT1 in wild-type, heterozygous, and homozygous DNMT1-M1 in mES, HeLa, and HS683 cells.

rather than increased vulnerability to proteasome degradation as the molecular mechanism for RFTS mutation–induced DNMT1 malfunction and neurodegenerative phenotypes.

The first key finding in our study is that both *Dnmt1* homozygous mutant mice are embryonic lethal, most likely because of loss of DNMT1 proteins. The defective homozygous mutant embryos were found at E10.5, but not E11, suggesting that the mutation causes embryonic lethality at a slightly later stage as *Dnmt1* knockout. Notably, the DNMT1 proteins were hardly detectable in defective *Dnmt1*$^{M2/M2}$ embryos. By using *Dnmt1*$^{+/-}$ mice as controls, we observed that the levels of DNMT1 proteins in both *Dnmt1*$^{+/M1}$ and *Dnmt1*$^{+/M2}$ heterozygous mutant mice were approximately half of the levels in wild-type mice and only slightly higher than those in *Dnmt1*$^{+/-}$ mice (Fig. 2 and figs. S1 and S2). This observation suggests that in *Dnmt1*$^{+/M1}$ and *Dnmt1*$^{+/M2}$ heterozygous mice, most of the mutant DNMT1 proteins are likely quickly degraded after synthesis and the remaining DNMT1 proteins are most likely the wild-type DNMT1. Thus, loss of mutant DNMT1 proteins

is most likely causal to embryonic lethality in homozygous mutant mice and neurodegenerative phenotypes in heterozygous mutants.

The second key finding in our study is that the heterozygous mutant mice show impaired adult neurogenesis and are defective in learning and memory and thus can be used as models for human HSAN1E diseases (Fig. 3). Both in vivo and in vitro BrdU labeling experiments revealed a reduced quantity of proliferative NSCs in heterozygous mutant mice (Fig. 3), and TUNEL assay revealed an increased cell death rate in the hippocampus of mutant mice (fig. S4). Extensive learning and memory tests of 4-month-old adult mice confirmed impaired cognitive function for the mutant mice. However, cognitive defects in mutant mice may not be as severe as reported in human patients, as the defects were modest and the mutant mice are grossly normal in growth, appearance, and life span. Although the full spectrum neuronal phenotypes of the mutant mice, including hearing, remain to be determined, these mice provide valuable models for further investigating neuronal defects in HSAN1E disease and how DNA methylation defect leads to human neuronal degenerative diseases.

The third key finding of our study is that the selective degradation of mutant DNMT1 proteins is most likely exerted via a specific proteinase cleavage event. Analysis of $Dnmt1^{+/+}$, $Dnmt1^{+/M1}$, and $Dnmt1^{M1/M1}$ mES cells allowed us to confirm a reduced protein stability for mutant DNMT1 (Fig. 4). However, neither proteasome inhibitor MG132 nor autophagy inhibitor CQ restored DNMT1 proteins in $Dnmt1^{M1/M1}$ mES to the levels in $Dnmt1^{+/+}$ ES cells, suggesting that the mutant DNMT1 proteins were not selectively degraded via proteasome and/or lysosome. Instead, we identified a specific truncated DNMT1 from $Dnmt1^{M1/M1}$ and $Dnmt1^{+/M2}$ mES cells (Fig. 5), indicating that both mutant DNMT1 proteins are subjected to this novel internal cleavage. As this truncated DNMT1 protein has a molecular weight of 75 to 80 kDa and migrated in SDS–polyacrylamide gel electrophoresis (SDS-PAGE) at position similar to that of FLAG-DNMT1 (amino acids 1 to 501), we concluded that the site(s) of cleavage is somewhere close to amino acid 501 within the region of RFTS domain. Because of lack of appropriate antibody, we have yet to identify whether the resulting C-terminal portion of DNMT1 protein exists in cells. Future effort is needed to map the exact C-terminal residue(s) of this truncated protein, as this may also provide clues as to which proteinase(s) may be involved in cleavage of mutant DNMT1.

The fourth key finding in our study is that it is the truncated DNMT1 protein, not the mutant DNMT1 protein per se, that is mislocalized to the nucleolus. Several lines of evidence support this conclusion. First, although DNMT1 nucleolus localization was observed only in mouse cells with *Dnmt1* mutation (Fig. 5), ectopically expressed DNMT1-M1 and DNMT-M2 mutants exhibited typical diffuse nuclear staining in both HeLa and mouse NIH3T3 cells (Fig. 6), indicating that the mutant DNMT1 proteins are not nucleolus localization by default. Second, various DNMT1 N-terminal fragments show nucleolus localization when expressed in HeLa cells (Fig. 6). Third, the same DNMT1-M1 mutation generated by base editing resulted in DNMT1 nucleolus localization in HS683 glioma cells (Fig. 6E) but not in HeLa cells (Fig. 7G), and the lack of DNMT1 nucleolus localization in HeLa cells correlates with the lack of 70- to 80-kDa truncated DNMT1. Together, we propose that the RFTS mutation is likely to affect DNMT1 conformation, which renders it vulnerable to a specific cleavage at the RFTS region by an unidentified proteinase. The resulting truncated N-terminal DNMT1 proteins mislocalize to nucleolus, presumably because of its aberrant protein folding. Numerous misfolded proteins have been shown to reside in the nucleolus (*42*–*44*). Consistently, a recent study has provided evidence for the nucleolus functioning as a phase-separated protein quality control compartment (*42*). In addition, protein aggregates have been broadly linked to neurodegenerative diseases in human and mouse models (*45*–*49*). The requirement for internal cleavage by a specific proteinase also can explain why the same DNMT1 mutation results in DNMT1 nucleolus mislocalization and growth defect in HS683 glioma cells but has no effect on DNMT1 in HeLa cells, as the proteinase required for mutant DNMT1 cleavage could be expressed in a cell type–specific manner, present in HS683 but absent in HeLa cells. Similarly, this model can also explain why we observed nucleolar mislocalization for endogenous DNMT1 proteins in $Dnmt1^{M1/M1}$ ES cells but not for ectopically expressed mutant DNMT1 proteins in NIH3T3 cells, as ectopically expressed DNMT1 could overwhelm the limited cleavage capacity of endogenous proteinase. The identification and characterization of this putative proteinase in the future would be the key to understand better how the RFTS mutations in DNMT1 lead to HSAN1E and ADCA-DN diseases.

An intriguing question regarding HSAN1E and ADCA-DN diseases is that all DNMT1 mutations identified thus far are clustered in the RFTS region (*32*, *33*). Although the RFTS mutations are likely to render DNMT1 proteins unstable as revealed by our study, however, the RFTS mutations are unlikely a group of pure loss-of-function DNMT1 mutations because, so far, no nonsense DNMT1 mutation within and outside of the RFTS region has been identified in patients with HSAN1E and ADCA-DN neurodegenerative disease. In other words, if the loss-of-function mutation were the driving force for HSAN1E and ADCA-DN neurodegenerative diseases, then nonsense DNMT1 mutation would be expected to sufficiently drive the diseases. We would therefore expect to see many more HSAN1E and ADCA-DN patients with DNMT1 nonsense mutation because these mutations would occur at much higher frequency than specific missense mutations in RFTS. Therefore, besides impaired function in DNA methylation, the RFTS mutations also must attribute to the pathogenesis by gain of function. In this regard, we are tempted to suggest that the nucleolar mislocalized truncated DNMT1 proteins may interfere with the appropriate function of nucleolus or other processes. We propose that the combination of effect of loss of function in DNA methylation and gain-of-function effect by truncated DNMT1 leads to pathogenesis of HSAN1E neurodegenerative diseases. In this regard, the mouse models generated in this study will be valuable for further investigations of the molecular mechanisms underlying the pathogenesis of HSAN1E and possibly the related ADCA-DN diseases.

MATERIALS AND METHODS

Plasmids

pcDNA3.1-FLAG-DNMT1, pcDNA3.1-Myc-DNMT1, pPYCAGIP-FLAG-DNMT1, and pPYCAGIP-UHRF1 were constructed in our laboratory as previously described (*19*, *50*, *51*). All mutants were generated by polymerase chain reaction (PCR)–based point mutagenesis strategy and verified by DNA sequencing. ABEmax and U6-sgRNA(sp)-EF1α-GFP plasmids were provided by Li Laboratory from East China Normal University.

Cell culture and transient transfection

HeLa, human embryonic kidney 293T, NIH3T3, MEF, and HS683 cells were grown in Dulbecco's modified Eagle's medium (DMEM) (Gibco) supplemented with 10% fetal bovine serum (FBS; Intergen) and 1% penicillin-streptomycin (Gibco). *Dnmt1*$^{+/+}$, *Dnmt1*$^{+/M1}$, *Dnmt1*$^{+/M2}$, and *Dnmt1*$^{M1/M1}$ mES cell lines were maintained on mitomycin C–treated MEFs and cultured in mES cell media (DMEM) supplemented with 15% FBS, leukaemia inhibitory factor (LIF) (1000 U/ml), penicillin (50 U/ml), streptomycin (50 μg/ml), 2 mM GlutaMAX, 0.1 mM nonessential amino acids, 1 mM sodium pyruvate, and 0.1 mM 2-mercaptoethanol. CGR8 mES cells were cultured in Glasgow's minimum essential medium (GMEM) supplemented with 15% FBS, LIF (1000 U/ml), streptomycin (50 μg/ml), 2 mM GlutaMAX, and 0.1 mM 2-mercaptoethanol. Cells were kept in 5% CO_2 and at 37°C. The medium was changed every other day. Plasmid transfection was performed using Lipofectamine 2000 (Invitrogen) according to the manufacturer's instructions.

Mouse strains

All *Dnmt1* mutation mice used were constructed in congenic C57BL/6 strain. *Dnmt1 M1* mutation c.1499A>G mice (Tyr500Cys) were generated by Cyagen Biosciences Inc. *Dnmt1* M2 mutation c.1486-1487CC>TA (Pro496Tyr) mice were constructed by in-house animal facility by coinjecting Cas9 mRNA, gRNA, and a donor oligo (M1 donor oligo sequence, 5′-CATTTGCTGAATACATTTT-GATGGAGCCCAGCAAAGAGTGTGAGCCAATATTTGGGCT-GATGCAGGAGAAAATTTACATCAGCAAGAT-3′; M2 donor oligo sequence, 5′-CATTTGCTGAATACATTTTGATGGAGTA-CAGCAAAGAGTATGAGCCAATATTTGGGCTGATGCAG-GAGAAAATTTACAT-3′) into fertilized eggs. *Dnmt1*$^{+/-}$ mice were provided by G. Xu's laboratory in Fudan University. All mice were housed at controlled temperature (25°C) and 12-hour light/12-hour dark cycle. All animal experiments conformed to the regulations drafted by the Association for Assessment and Accreditation of Laboratory Animal Care in Shanghai and were approved by either the East China Normal University Center for Animal Research or the Institutional Animal Care and Use Committee of Zhejiang University.

BrdU pulse labeling

To evaluate the percentage of cell proliferation and differentiation of *Dnmt1*$^{+/+}$ and *Dnmt1*$^{+/M2}$ mice in vivo, 4-month-old male mice were intraperitoneally injected with BrdU (50 mg/kg). To assess the proliferation of aNSCs, BrdU was injected every 4 hours six consecutive times within 24 hours. Four hours after the last injection of BrdU, the mice were sacrificed by perfusion and the brains were taken for frozen sections. To assess the differentiation of aNSCs, the other two batches of mice were given BrdU for three consecutive days (twice daily at 10-hour intervals). Mice were sacrificed at 4 weeks after the final BrdU injection for frozen sections.

Immunohistochemistry

Four-month-old male mice were perfused with 4% paraformaldehyde. Brains were gently removed and postfixed in 4% paraformaldehyde at 4°C for 24 hours. The brain samples were then transferred into 30% sucrose solution at 4°C for dehydration. The brain samples were embedded in optimal cutting temperature (Thermo Fisher Scientific) and sectioned in the coronal plane with a cryostat 20 μm thick and collected at 150-μm intervals. Six sections per brain were analyzed, and consecutive sections of brain were used for BrdU, DCX, and NeuN staining. VECTASTAIN kit (Vector Laboratories) was used to perform BrdU and DCX staining according to the manufacturer's directions. For BrdU, DCX, and NeuN stainings, BrdU (Sigma-Aldrich, B8434), DCX (Cell Signaling Technology, no. 4604), and NeuN (Millipore, MAB377) antibodies were used, respectively. The plaque numbers and BrdU and DCX staining were quantified using ImageJ program. All immunostaining experiments were repeated with sections from at least three animals of each genotype.

Western blotting

Mouse tissues were homogenized in radioimmunoprecipitation assay (RIPA) buffer [50 mM tris-HCl (pH 8.0), 1 mM EDTA, 0.1% SDS, 150 mM NaCl, 1% NP-40, and 0.1% sodium deoxycholate] including cOmplete Protease Inhibitor mixture (Roche) and centrifuged, and 100 μg of the supernatant was loaded onto 8 to 10% gradient SDS-PAGE gels and immunoblotted with anti-DNMT1 (Abcam, ab87654), UHRF1 (homemade), β-actin (Sigma-Aldrich, A5441), glyceraldehyde-3-phosphate dehydrogenase (Abmart, M20006L), p53 (Cell Signaling Technology, mAb no. 2524), and autophagy-related protein LC3 A (LC3) (Sigma-Aldrich, L7543) antibodies. For WB using cells, cells were harvested and extracted in RIPA buffer as explained above. WB experiments were performed with at least three mice from each genotype, and representative data were shown.

Immunoprecipitation

To enrich the endogenous truncated proteins of DNMT1, the cell lysates derived from *Dnmt1*$^{+/+}$, *Dnmt1*$^{+/M2}$, or *Dnmt1*$^{M1/M1}$ mES cells were incubated with the DNMT1 antibody (Abcam, ab87654) covalently cross-linked to protein A agarose beads. To determine the interaction of DNMT1 and UHRF1, lysate supernatant of 293T overexpressing FLAG-DNMT and UHRF1 were incubated with anti-FLAG M2 agarose beads. The immunoprecipitated proteins were then boiled in 1× SDS loading buffer and analyzed by WB as described.

Morris water maze test

The Morris water maze testing procedure has been described previously (*52*, *53*). Six to 10 mice from each indicated genotype were trained to find the visible platform three trials a day for the first day and tested to find the hidden platform for seven consecutive days. In each trial, the mice were allowed to swim until it found the hidden platform or until 2 min had elapsed, and at which point, the mouse was guided to the platform. The mouse was then allowed to sit on the platform for 10 s before being picked up. During the test days, the platform was hidden 1 cm beneath the water. The escape latency was recorded by a video camera. The experimenter was blind to the genotypes of the mice. The swim speed of each mouse was calculated by video tracking system and MATLAB software.

Eight-arm radial water maze test

Six to 10 4-month-old male mice from each indicated genotype (*Dnmt1*$^{+/+}$ and *Dnmt1*$^{+/M2}$) were trained. The eight-arm radial water maze testing procedure has been described previously (*53*). The apparatus consisted of an octagonal platform (60-mm side length) in the center and eight identical extending arms (300 mm by 60 mm by 150 mm). Arms were made of transparent Plexiglas to allow the animal to see visual cues placed in the room. Doors (25 cm high) were located at the entrance of each arm, with dual sensors to detect the animal when all four paws crossed the door. Each arm

was equipped with a head-end detector at the end where chocolate was placed to attract the mice. A video tracking system (Med Associates Inc.) was used to observe the movement of the mice. Several salient visual cues (a star, a rectangle, a circle, and a triangle) hung constantly on the white wall in the same positions, and an incandescent light bulb was above the apparatus to prevent shadow within the maze. Animals were fasting 24 hours before training, and each animal was weighed before and after fasting to adjust the body weight to 80 to 85% of normal, free-eating animals. On the first day, they were placed in the full-baited maze in which chocolate particles were scattered in the center and the end of the arms in groups of four for 10 min, and animals could explore the maze freely to eat the food rewards with all doors opened. On the second and third days, each mouse was put into the maze alone, with chocolate placed only at the ends of the arms. Mice were placed on the center platform for 10 s and allowed to move freely for 10 min or until all chocolate pellets were consumed. During these days, animals were induced to find and eat food only once in each arm. For the next days, only four arms were baited, and food was placed at the end of the same four arms during this session. Mice were allowed to move freely until all chocolate pellets were consumed or the trial lasted for more than 10 min. A reference memory error was counted when animals visited a nonbaited arm with all four paws, and working memory was counted when animals went into an arm that was visited previously with all four paws. The maze was cleaned between each mouse to minimize olfactory intramaze cues.

RNA isolation and analysis

Total RNA from mouse tissues was isolated by using TRIzol (QIAGEN). For real-time quantitative PCR analysis, cDNA was synthesized from total RNA by SuperScript III reverse transcriptase (Invitrogen) with random primers. The cDNA was then subjected to PCR analysis with gene-specific primers in the presence of SYBR Green (Bio-Rad). Relative abundance of mRNA was obtained by normalization to β-actin levels.

Immunofluorescence staining

For immunofluorescent staining assay, the cultured cells were washed twice in phosphate-buffered saline (PBS) and then fixed in 4% paraformaldehyde for 20 min at room temperature. Fixed cells were washed with PBS containing 0.1% Triton X-100 and incubated with blocking buffer (PBS containing 0.1% Triton X-100 and 5% FBS) for 1 hour at 37°C. After blocking, primary antibodies were added and incubated with the cells overnight at 4°C. The cells were then washed 4× for 10 min with PBS containing 0.1% Triton X-100 before incubation with secondary antibodies (diluted 1:500) for 1 hour in the dark and at 37°C. Last, cells were washed 5 × 10 min with PBS containing 0.1% Triton X-100, stained with 4′,6-diamidino-2-phenylindole, and stored in PBS in the dark at 4°C until imaging. The primary antibodies used were as follows: DNMT1 (Abcam, ab87654), FLAG (Sigma-Aldrich, F7425), UBF (Santa Cruz Biotechnology, sc-13125), nucleolin (homemade polyclonal antibody), SOX2 (Abcam, ab-97959), GFAP (Dako, Z0334), and Tuj1 (Promega, G712A). The following secondary antibodies were used: Alexa Fluor 680 goat anti-rabbit immunoglobulin G (IgG) (Jackson ImmunoResearch, 111-625-144), Alexa Fluor 790 goat anti-mouse IgG (Jackson ImmunoResearch, 115-655-146), Alexa Fluor 594 goat anti-rabbit IgG (Jackson ImmunoResearch, 111-585-003), and Alexa Fluor 488 goat anti-mouse IgG (Jackson ImmunoResearch, 115-545-003).

EdU staining assay

The EdU staining assay for identification of S phase cells was performed according to the Cell-Light EdU Fluorescent Detection Kit (RiboBio, Guangzhou, China, C10310) with a slight modification. Briefly, cells grown on 48-well plates were labeled with 20 μM EdU for approximately 2 hours at 37°C, washed with 1× PBS twice, and fixed with 4% paraformaldehyde for 20 min at 4°C before neutralization with glycine (2 mg/ml). Then, the cells were permeabilized, blocked, and incubated with antibodies as described above. Last, the EdU were stained by Apollo reaction buffer at 37°C for 30 min. Slides were washed by methanol once and PBS twice before fluorescent imaging.

DNA methylation analysis by HPLC

Preparation of genomic DNA, DNA hydrolysis, and measurement of deoxycytidine monophosphate (dCMP) and 2′-desoxy-5-methylcytidine-3′-monophosphate (5me-dCMP) by HPLC were performed as described (*54*). Briefly, genomic DNA was prepared from mES cells, HeLa cells, or various mouse tissues. The RNA-free genomic DNA samples were treated with nuclease P1 (Wako) and cloned alkaline phosphatase (CIAP, New England Biolabs) before they were subjected to HPLC (Agilent 2000 Series, Agilent Eclipse XDB-C18) analysis.

Protein stability analysis

Measurement of DNMT1 protein stability with block of new protein synthesis by cycloheximide was performed essentially as described (*55*). Briefly, the half-life of endogenous or ectopically expressing DNMT1 was determined by cycloheximide chase assay. Cells were seeded in 12-well plates. After adhering, cells were treated with cycloheximide (100 μg/ml) and collected at the indicated time points, and the levels of DNMT1 were then subjected to WB analysis and quantified by using ImageJ software.

Preparation of mES cell lines from wild-type and mutant embryos

The mES cell lines were derived from mouse blastocysts isolated from E3.5 embryos as previously described (*56*, *57*). Briefly, female mice were induced to superovulate by injecting 5 U of pregnant mare's serum gonadotropin followed by 5 U of human chorionic gonadotropin (hCG) with an interval of 48 hours. They were caged with male mice immediately after the hCG injection for one night. Females with vaginal plug were designated to be at 0.5 days of pregnancy at noon of that day. Blastocysts (3.5 days old) were collected by flushing the uterus with PBS and cultured for 3 to 4 days in DMEM as described on "feeder cell layer preparation" section. Inner cell masses that emerged from attached embryos were picked out, partially dissociated with trypsin, and transferred to a 24-well tissue culture plate. They were subcultured at an interval of 2 to 3 days to increasingly larger plates and dishes. Colonies containing cells of stem cell–like morphology were picked out and cultured individually to establish the stable mES cell lines.

Feeder cell layer preparation

Fibroblasts were derived from 12.5-day-old fetuses and cultured in DMEM with 10% FBS (Intergen) and 1% penicillin-streptomycin (Gibco). MEF cells were isolated as previously described (*58*). Briefly, primary culture of embryonic fibroblasts was obtained from 12.5- to 14.5-day-old fetuses of C57BL/C strain mice by mincing and trypsinization. Feeder cell layer was prepared by seeding culture dishes

with the fibroblasts at a density close to the confluency and treating them with mitomycin C (10 μg/ml; Wako Pure Chemicals Industries Ltd.) for 1 hour, followed by rinsing with the PBS three times.

Isolation and culture of aNSCs

The isolation of NSCs from the forebrain of adult mice (*59*, *60*) was performed as described previously. aNSCs were cultured in DMEM/F-12 medium containing fibroblast growth factor 2 (20 ng/ml; catalog no. 100-18B-B; PeproTech, Rocky Hill, NJ), epidermal growth factor (20 ng/ml; catalog no. 100-15; PeproTech), 2% B27 supplement (catalog no. 12587-010; Thermo Fisher Scientific, Grand Island, NY), 1% antibiotic-antimycotic (catalog no. 15140-122; Thermo Fisher Scientific), and 2 mM L-glutamine (catalog no. 25030-149; Thermo Fisher Scientific) in a 5% CO_2 incubator at 37°C.

RNA-seq analysis of aNSCs

aNSCs were isolated from three pairs of *Dnmt1*$^{+/+}$ and *Dnmt1*$^{+/M2}$ littermate mice as above. The RNA-seq profiling and data analysis were as described (*61*).

Proliferation and differentiation of NSCs in vitro

The proliferation and differentiation of NSCs were performed as described previously (*62*). Briefly, for the in vitro proliferation assay, aNSCs were cultured on coverslips with medium supplied with 5 mM BrdU for 8 hours. For the in vitro differentiation assay, aNSCs were cultured on coverslips with proliferation medium and then transferred into differentiation medium containing 1 mM retinoic acid (catalog no. R-2625, Sigma-Aldrich, Saint Louis, MO) and 5 mM forskolin (catalog no. F-6886, Sigma-Aldrich) for 48 hours.

Construction of DNMT1-M1 knock-in cell lines by base editing

DNMT1 knock-in (Dnmt1 M1 mutation c.1499A>G) cells were constructed using the base editing technology as described (*63*) with the following gRNA, CCGAGTATGCGCCCATATTT for DNMT1. Briefly, the single gRNA (sgRNA) sequence was first constructed into the U6-sgRNA(sp)-EF1α-GFP plasmid, and then, the ABEmax and U6-sgRNA(sp)-EF1α-GFP plasmids were transfected into target cells accordingly. Three to 5 days after transfection, the cells were harvested for genotyping by DNA sequencing and isolation of monoclonal cell lines by single-cell sorting.

Statistical analysis

All statistical tests were performed using the paired or unpaired Student's *t* test, and $P < 0.05$ was considered as statistically significant. In all the results, $^{*}P < 0.05$, $^{**}P < 0.01$, and "ns" denotes no significant difference.

SUPPLEMENTARY MATERIALS

Supplementary material for this article is available at https://science.org/doi/10.1126/sciadv.abe8511

View/request a protocol for this paper from *Bio-protocol*.

REFERENCES AND NOTES

1. R. Jaenisch, A. Bird, Epigenetic regulation of gene expression: How the genome integrates intrinsic and environmental signals. *Nat. Genet.* **33**, 245–254 (2003).
2. P. A. Jones, Functions of DNA methylation: Islands, start sites, gene bodies and beyond. *Nat. Rev. Genet.* **13**, 484–492 (2012).
3. J. A. Law, S. E. Jacobsen, Establishing, maintaining and modifying DNA methylation patterns in plants and animals. *Nat. Rev. Genet.* **11**, 204–220 (2010).
4. G. Fan, C. Beard, R. Z. Chen, G. Csankovszki, Y. Sun, M. Siniaia, D. Biniszkiewicz, B. Bates, P. P. Lee, R. Kühn, A. Trumpp, C.-S. Poon, C. B. Wilson, R. Jaenisch, DNA hypomethylation perturbs the function and survival of CNS neurons in postnatal animals. *J. Neurosci.* **21**, 788–797 (2001).
5. D. K. Ma, M. C. Marchetto, J. U. Guo, G.-l. Ming, F. H. Gage, H. Song, Epigenetic choreographers of neurogenesis in the adult mammalian brain. *Nat. Neurosci.* **13**, 1338–1344 (2010).
6. D. D. De Carvalho, J. S. You, P. A. Jones, DNA methylation and cellular reprogramming. *Trends Cell Biol.* **20**, 609–617 (2010).
7. P. A. Jones, G. Liang, Rethinking how DNA methylation patterns are maintained. *Nat. Rev. Genet.* **10**, 805–811 (2009).
8. T. Chen, E. Li, Structure and function of eukaryotic DNA methyltransferases. *Curr. Top. Dev. Biol.* **60**, 55–89 (2004).
9. H. Gujar, D. J. Weisenberger, G. Liang, The roles of human DNA methyltransferases and their isoforms in shaping the epigenome. *Genes* **10**, 172 (2019).
10. H. Leonhardt, A. W. Page, H.-U. Weier, T. H. Bestor, A targeting sequence directs DNA methyltransferase to sites of DNA replication in mammalian nuclei. *Cell* **71**, 865–873 (1992).
11. W. Qin, P. Wolf, N. Liu, S. Link, M. Smets, F. La Mastra, I. Forné, G. Pichler, D. Hörl, K. Fellinger, F. Spada, I. M. Bonapace, A. Imhof, H. Harz, H. Leonhardt, DNA methylation requires a DNMT1 ubiquitin interacting motif (UIM) and histone ubiquitination. *Cell Res.* **25**, 911–929 (2015).
12. M. Bostick, J. K. Kim, P.-O. Estève, A. Clark, S. Pradhan, S. E. Jacobsen, UHRF1 plays a role in maintaining DNA methylation in mammalian cells. *Science* **317**, 1760–1764 (2007).
13. J. Sharif, M. Muto, S.-i. Takebayashi, I. Suetake, A. Iwamatsu, T. A. Endo, J. Shinga, Y. Mizutani-Koseki, T. Toyoda, K. Okamura, S. Tajima, K. Mitsuya, M. Okano, H. Koseki, The SRA protein Np95 mediates epigenetic inheritance by recruiting Dnmt1 to methylated DNA. *Nature* **450**, 908–912 (2007).
14. H. Hashimoto, J. R. Horton, X. Zhang, M. Bostick, S. E. Jacobsen, X. Cheng, The SRA domain of UHRF1 flips 5-methylcytosine out of the DNA helix. *Nature* **455**, 826–829 (2008).
15. P. Karagianni, L. Amazit, J. Qin, J. Wong, ICBP90, a novel methyl K9 H3 binding protein linking protein ubiquitination with heterochromatin formation. *Mol. Cell. Biol.* **28**, 705–717 (2008).
16. A. Rottach, C. Frauer, G. Pichler, I. M. Bonapace, F. Spada, H. Leonhardt, The multi-domain protein Np95 connects DNA methylation and histone modification. *Nucleic Acids Res.* **38**, 1796–1804 (2010).
17. K. Arita, M. Ariyoshi, H. Tochio, Y. Nakamura, M. Shirakawa, Recognition of hemi-methylated DNA by the SRA protein UHRF1 by a base-flipping mechanism. *Nature* **455**, 818–821 (2008).
18. G. V. Avvakumov, J. R. Walker, S. Xue, Y. Li, S. Duan, C. Bronner, C. H. Arrowsmith, S. Dhe-Paganon, Structural basis for recognition of hemi-methylated DNA by the SRA domain of human UHRF1. *Nature* **455**, 822–825 (2008).
19. X. Liu, Q. Gao, P. Li, Q. Zhao, J. Zhang, J. Li, H. Koseki, J. Wong, UHRF1 targets DNMT1 for DNA methylation through cooperative binding of hemi-methylated DNA and methylated H3K9. *Nat. Commun.* **4**, 1563 (2013).
20. E. Citterio, R. Papait, F. Nicassio, M. Vecchi, P. Gomiero, R. Mantovani, P. P. Di Fiore, I. M. Bonapace, Np95 is a histone-binding protein endowed with ubiquitin ligase activity. *Mol. Cell. Biol.* **24**, 2526–2535 (2004).
21. E. Rajakumara, Z. Wang, H. Ma, L. Hu, H. Chen, Y. Lin, R. Guo, F. Wu, H. Li, F. Lan, Y. G. Shi, Y. Xu, D. J. Patel, Y. Shi, PHD finger recognition of unmodified histone H3R2 links UHRF1 to regulation of euchromatic gene expression. *Mol. Cell* **43**, 275–284 (2011).
22. S. B. Rothbart, B. M. Dickson, M. S. Ong, K. Krajewski, S. Houliston, D. B. Kireev, C. H. Arrowsmith, B. D. Strahl, Multivalent histone engagement by the linked tandem Tudor and PHD domains of UHRF1 is required for the epigenetic inheritance of DNA methylation. *Genes Dev.* **27**, 1288–1298 (2013).
23. L. Ferry, A. Fournier, T. Tsusaka, G. Adelmant, T. Shimazu, S. Matano, O. Kirsh, R. Amouroux, N. Dohmae, T. Suzuki, G. J. Filion, W. Deng, M. de Dieuleveult, L. Fritsch, S. Kudithipudi, A. Jeltsch, H. Leonhardt, P. Hajkova, J. A. Marto, K. Arita, Y. Shinkai, P.-A. Defossez, Methylation of DNA ligase 1 by G9a/GLP recruits UHRF1 to replicating DNA and regulates DNA methylation. *Mol. Cell* **67**, 550–565.e5 (2017).
24. A. Nishiyama, L. Yamaguchi, J. Sharif, Y. Johmura, T. Kawamura, K. Nakanishi, S. Shimamura, K. Arita, T. Kodama, F. Ishikawa, H. Koseki, M. Nakanishi, Uhrf1-dependent H3K23 ubiquitylation couples maintenance DNA methylation and replication. *Nature* **502**, 249–253 (2013).
25. J. Li, R. Wang, J. Jin, M. Han, Z. Chen, Y. Gao, X. Hu, H. Zhu, H. Gao, K. Lu, Y. Shao, C. Lyu, W. Lai, P. Li, G. Hu, J. Li, D. Li, H. Wang, Q. Wu, J. Wong, USP7 negatively controls global DNA methylation by attenuating ubiquitinated histone-dependent DNMT1 recruitment. *Cell Discov.* **6**, 58 (2020).
26. A. Nishiyama, C. B. Mulholland, S. Bultmann, S. Kori, A. Endo, Y. Saeki, W. Qin, C. Trummer, Y. Chiba, H. Yokoyama, S. Kumamoto, T. Kawakami, H. Hojo, G. Nagae, H. Aburatani,

K. Tanaka, K. Arita, H. Leonhardt, M. Nakanishi, Two distinct modes of DNMT1 recruitment ensure stable maintenance DNA methylation. *Nat. Commun.* **11**, 1222 (2020).
27. E. Li, T. H. Bestor, R. Jaenisch, Targeted mutation of the DNA methyltransferase gene results in embryonic lethality. *Cell* **69**, 915–926 (1992).
28. P. Golshani, L. Hutnick, F. Schweizer, G. Fan, Conditional Dnmt1 deletion in dorsal forebrain disrupts development of somatosensory barrel cortex and thalamocortical long-term potentiation. *Thalamus Relat. Syst.* **3**, 227–233 (2005).
29. H. Noguchi, A. Kimura, N. Murao, M. Namihira, K. Nakashima, Prenatal deletion of *DNA methyltransferase 1* in neural stem cells impairs neurogenesis and causes anxiety-like behavior in adulthood. *Neurogenesis* **3**, e1232679 (2016).
30. C. J. Klein, M. V. Botuyan, Y. Wu, C. J. Ward, G. A. Nicholson, S. Hammans, K. Hojo, H. Yamanishi, A. R. Karpf, D. C. Wallace, M. Simon, C. Lander, L. A. Boardman, J. M. Cunningham, G. E. Smith, W. J. Litchy, B. Boes, E. J. Atkinson, S. Middha, P. J. B. Dyck, J. E. Parisi, G. Mer, D. I. Smith, P. J. Dyck, Mutations in DNMT1 cause hereditary sensory neuropathy with dementia and hearing loss. *Nat. Genet.* **43**, 595–600 (2011).
31. J. Winkelmann, L. Lin, B. Schormair, B. R. Kornum, J. Faraco, G. Plazzi, A. Melberg, F. Cornelio, A. E. Urban, F. Pizza, F. Poli, F. Grubert, T. Wieland, E. Graf, J. Hallmayer, T. M. Strom, E. Mignot, Mutations in DNMT1 cause autosomal dominant cerebellar ataxia, deafness and narcolepsy. *Hum. Mol. Genet.* **21**, 2205–2210 (2012).
32. J. Baets, X. Duan, Y. Wu, G. Smith, W. W. Seeley, I. Mademan, N. M. McGrath, N. C. Beadell, J. Khoury, M.-V. Botuyan, G. Mer, G. A. Worrell, K. Hojo, J. DeLeon, M. Laura, Y.-T. Liu, J. Senderek, J. Weis, P. V. D. Bergh, S. L. Merrill, M. M. Reilly, H. Houlden, M. Grossman, S. S. Scherer, P. D. Jonghe, P. J. Dyck, C. J. Klein, Defects of mutant DNMT1 are linked to a spectrum of neurological disorders. *Brain* **138**, 845–861 (2015).
33. A. B. Norvil, D. Saha, M. S. Dar, H. Gowher, Effect of disease-associated germline mutations on structure function relationship of DNA methyltransferases. *Genes* **10**, 369 (2019).
34. M. Smets, S. Link, P. Wolf, K. Schneider, V. Solis, J. Ryan, D. Meilinger, W. Qin, H. Leonhardt, DNMT1 mutations found in HSANIE patients affect interaction with UHRF1 and neuronal differentiation. *Hum. Mol. Genet.* **26**, 1522–1534 (2017).
35. H. Miura, R. M. Quadros, C. B. Gurumurthy, M. Ohtsuka, Easi-CRISPR for creating knock-in and conditional knockout mouse models using long ssDNA donors. *Nat. Protoc.* **13**, 195–215 (2018).
36. Z. Sun, Y. Wu, T. Ordog, S. Baheti, J. Nie, X. Duan, K. Hojo, J. P. Kocher, P. J. Dyck, C. J. Klein, Aberrant signature methylome by DNMT1 hot spot mutation in hereditary sensory and autonomic neuropathy 1E. *Epigenetics* **9**, 1184–1193 (2014).
37. C. D. Clelland, M. Choi, C. Romberg, G. D. Clemenson, A. Fragniere, P. Tyers, S. Jessberger, L. M. Saksida, R. A. Barker, F. H. Gage, T. J. Bussey, A functional role for adult hippocampal neurogenesis in spatial pattern separation. *Science* **325**, 210–213 (2009).
38. A. Sahay, K. N. Scobie, A. S. Hill, C. M. O'Carroll, M. A. Kheirbek, N. S. Burghardt, A. A. Fenton, A. Dranovsky, R. Hen, Increasing adult hippocampal neurogenesis is sufficient to improve pattern separation. *Nature* **472**, 466–470 (2011).
39. W. Deng, J. B. Aimone, F. H. Gage, New neurons and new memories: How does adult hippocampal neurogenesis affect learning and memory? *Nat. Rev. Neurosci.* **11**, 339–350 (2010).
40. G. Egger, S. Jeong, S. G. Escobar, C. C. Cortez, T. W. H. Li, Y. Saito, C. B. Yoo, P. A. Jones, G. Liang, Identification of DNMT1 (DNA methyltransferase 1) hypomorphs in somatic knockouts suggests an essential role for DNMT1 in cell survival. *Proc. Natl. Acad. Sci. U.S.A.* **103**, 14080–14085 (2006).
41. T. Chen, S. Hevi, F. Gay, N. Tsujimoto, T. He, B. Zhang, Y. Ueda, E. Li, Complete inactivation of DNMT1 leads to mitotic catastrophe in human cancer cells. *Nat. Genet.* **39**, 391–396 (2007).
42. F. Frottin, F. Schueder, S. Tiwary, R. Gupta, R. Körner, T. Schlichthaerle, J. Cox, R. Jungmann, F. U. Hartl, M. S. Hipp, The nucleolus functions as a phase-separated protein quality control compartment. *Science* **365**, 342–347 (2019).
43. M. Azkanaz, A. R. López, B. d. Boer, W. Huiting, P.-O. Angrand, E. Vellenga, H. H. Kampinga, S. Bergink, J. H. Martens, J. J. Schuringa, V. van den Boom, Protein quality control in the nucleolus safeguards recovery of epigenetic regulators after heat shock. *eLife* **8**, e45205 (2019).
44. L. Latonen, Phase-to-phase with nucleoli—Stress responses, protein aggregation and novel roles of RNA. *Front. Cell. Neurosci.* **13**, 151 (2019).
45. F. Trettel, D. Rigamonti, P. Hilditch-Maguire, V. C. Wheeler, A. H. Sharp, F. Persichetti, E. Cattaneo, M. E. MacDonald, Dominant phenotypes produced by the *HD* mutation in STH*dh*^{Q111} striatal cells. *Hum. Mol. Genet.* **9**, 2799–2809 (2000).
46. I. Kwon, S. Xiang, M. Kato, L. Wu, P. Theodoropoulos, T. Wang, J. Kim, J. Yun, Y. Xie, S. L. McKnight, Poly-dipeptides encoded by the C9orf72 repeats bind nucleoli, impede RNA biogenesis, and kill cells. *Science* **345**, 1139–1145 (2014).
47. K. H. Lee, P. Zhang, H. J. Kim, D. M. Mitrea, M. Sarkar, B. D. Freibaum, J. Cika, M. Coughlin, J. Messing, A. Molliex, B. A. Maxwell, N. C. Kim, J. Temirov, J. Moore, R. M. Kolaitis, T. I. Shaw, B. Bai, J. Peng, R. W. Kriwacki, J. P. Taylor, C9orf72 dipeptide repeats impair the assembly, dynamics, and function of membrane-less organelles. *Cell* **167**, 774–788.e17 (2016).
48. G. B. Irvine, O. M. El-Agnaf, G. M. Shankar, D. M. Walsh, Protein aggregation in the brain: The molecular basis for Alzheimer's and Parkinson's diseases. *Mol. Med.* **14**, 451–464 (2008).
49. E. H. Koo, P. T. Lansbury, J. W. Kelly, Amyloid diseases: Abnormal protein aggregation in neurodegeneration. *Proc. Natl. Acad. Sci. U.S.A.* **96**, 9989–9990 (1999).
50. J. Zhang, Q. Gao, P. Li, X. Liu, Y. Jia, W. Wu, J. Li, S. Dong, H. Koseki, J. Wong, S phase-dependent interaction with DNMT1 dictates the role of UHRF1 but not UHRF2 in DNA methylation maintenance. *Cell Res.* **21**, 1723–1739 (2011).
51. Z. Yang, J. Jiang, D. M. Stewart, S. Qi, K. Yamane, J. Li, Y. Zhang, J. Wong, AOF1 is a histone H3K4 demethylase possessing demethylase activity-independent repression function. *Cell Res.* **20**, 276–287 (2010).
52. K. J. Bryan, H.-g. Lee, G. Perry, M. A. Smith, G. Casadesus, Transgenic mouse models of Alzheimer's disease: Behavioral testing and considerations, in *Methods of Behavior Analysis in Neuroscience* (CRC Press, ed. 2, 2009).
53. L. Li, L. Zang, F. Zhang, J. Chen, H. Shen, L. Shu, F. Liang, C. Feng, D. Chen, H. Tao, T. Xu, Z. Li, Y. Kang, H. Wu, L. Tang, P. Zhang, P. Jin, Q. Shu, X. Li, Fat mass and obesity-associated (FTO) protein regulates adult neurogenesis. *Hum. Mol. Genet.* **26**, 2398–2411 (2017).
54. Q. Zhao, J. Zhang, R. Chen, L. Wang, B. Li, H. Cheng, X. Duan, H. Zhu, W. Wei, J. Li, Q. Wu, J.-D. J. Han, W. Yu, S. Gao, G. Li, J. Wong, Dissecting the precise role of H3K9 methylation in crosstalk with DNA maintenance methylation in mammals. *Nat. Commun.* **7**, 12464–12464 (2016).
55. G. Ding, P. Chen, H. Zhang, X. Huang, Y. Zang, J. Li, J. Li, J. Wong, Regulation of ubiquitin-like with plant homeodomain and RING finger domain 1 (UHRF1) protein stability by heat shock protein 90 chaperone machinery. *J. Biol. Chem.* **291**, 20125–20135 (2016).
56. H. Suemori, N. Nakatsuji, Establishment of the embryo-derived stem (ES) cell lines from mouse blastocysts: Effects of the feeder cell layer. *Dev. Growth Differ.* **29**, 133–139 (1987).
57. M. J. Evans, M. H. Kaufman, Establishment in culture of pluripotential cells from mouse embryos. *Nature* **292**, 154–156 (1981).
58. D. A. Conner, Mouse embryo fibroblast (MEF) feeder cell preparation. *Curr. Protoc. Mol. Biol.* **51**, 23.2.1–23.2.7 (2001).
59. X. Li, B. Yao, L. Chen, Y. Kang, Y. Li, Y. Cheng, L. Li, L. Lin, Z. Wang, M. Wang, F. Pan, Q. Dai, W. Zhang, H. Wu, Q. Shu, Z. Qin, C. He, M. Xu, P. Jin, Ten-eleven translocation 2 interacts with forkhead box O3 and regulates adult neurogenesis. *Nat. Commun.* **8**, 15903–15903 (2017).
60. K. E. Szulwach, X. Li, R. D. Smrt, Y. Li, Y. Luo, L. Lin, N. J. Santistevan, W. Li, X. Zhao, P. Jin, Cross talk between microRNA and epigenetic regulation in adult neurogenesis. *J. Cell Biol.* **189**, 127–141 (2010).
61. M. Han, J. Li, Y. Cao, Y. Huang, W. Li, H. Zhu, Q. Zhao, J. J. Han, Q. Wu, J. Li, J. Feng, J. Wong, A role for LSH in facilitating DNA methylation by DNMT1 through enhancing UHRF1 chromatin association. *Nucleic Acids Res.* **48**, 12116–12134 (2020).
62. J. Chen, Y.-C. Zhang, C. Huang, H. Shen, B. Sun, X. Cheng, Y.-J. Zhang, Y.-G. Yang, Q. Shu, Y. Yang, X. Li, m^{6}A regulates neurogenesis and neuronal development by modulating histone methyltransferase Ezh2. *Genomics Proteomics Bioinformatics* **17**, 154–168 (2019).
63. N. M. Gaudelli, A. C. Komor, H. A. Rees, M. S. Packer, A. H. Badran, D. I. Bryson, D. R. Liu, Programmable base editing of A•T to G•C in genomic DNA without DNA cleavage. *Nature* **551**, 464–471 (2017).

Acknowledgments: We thank members of the laboratory of J.W. for valuable discussion. We also thank Q. Sun for assistance in TUNEL assay and X. Wang for analysis of RNA-seq data. **Funding:** This study is supported by grants from the National Natural Science Foundation of China (31730048 and 81530078 to J.W., 31771395 to X.L., and 31900453 to Jialun Li), the Ministry of Science and Technology of China (2017YFA054201), and the National Key Research and Development Program of China (2017YFE0196600 to X.L.). **Author contributions:** W.W. generated all *Dnmt1*$^{+/+}$, *Dnmt1*$^{+/M1}$, *Dnmt1*$^{+/M2}$, or *Dnmt1*$^{M1/M1}$ mES cells; DNMT1$^{+/+}$, DNMT1$^{+/M1}$, or DNMT1$^{M1/M1}$ HeLa cells; and *Dnmt1*$^{+/+}$ and *Dnmt1*$^{+/M2}$ MEF cells. W.W., X.D., Y.W., and Jialun Li performed various biochemical analyses of cell and mice. X.Z. and S.Q. carried out behavioral analysis of the mice and analyzed the proliferation and differentiation of mouse NSCs in vivo and in vitro and cell death assay. Y.S. and M.L. constructed the Dnmt1 M2 mouse model. Jiwen Li, X.L., and J.W. supervised the project, and X.L. and J.W. wrote the manuscript. **Competing interests:** The authors declare that they have no competing interests. **Data and materials availability:** All data needed to evaluate the conclusions in the paper are present in the paper and/or the Supplementary Materials. The *Dnmt1-M1* and *Dnmt1-M2* mutant mice can be provided by East China Animal Core Facility pending scientific review and a completed material transfer agreement. Requests for the mouse models should be submitted to J.W.

Submitted 18 September 2020
Accepted 12 July 2021
Published 1 September 2021
10.1126/sciadv.abe8511

Citation: W. Wang, X. Zhao, Y. Shao, X. Duan, Y. Wang, J. Li, J. Li, D. Li, X. Li, J. Wong, Mutation-induced DNMT1 cleavage drives neurodegenerative disease. *Sci. Adv.* **7**, eabe8511 (2021).